



저작자표시-비영리-변경금지 2.0 대한민국

이용자는 아래의 조건을 따르는 경우에 한하여 자유롭게

- 이 저작물을 복제, 배포, 전송, 전시, 공연 및 방송할 수 있습니다.

다음과 같은 조건을 따라야 합니다:



저작자표시. 귀하는 원 저작자를 표시하여야 합니다.



비영리. 귀하는 이 저작물을 영리 목적으로 이용할 수 없습니다.



변경금지. 귀하는 이 저작물을 개작, 변형 또는 가공할 수 없습니다.

- 귀하는, 이 저작물의 재이용이나 배포의 경우, 이 저작물에 적용된 이용허락조건을 명확하게 나타내어야 합니다.
- 저작권자로부터 별도의 허가를 받으면 이러한 조건들은 적용되지 않습니다.

저작권법에 따른 이용자의 권리와 책임은 위의 내용에 의하여 영향을 받지 않습니다.

이것은 [이용허락규약\(Legal Code\)](#)을 이해하기 쉽게 요약한 것입니다.

[Disclaimer](#)



공학박사 학위논문

Design and Analysis of Silicon and Titanium Dioxide Anodes for Lithium-ion Batteries

리튬이온전지용 고용량 음극 재료의

심화 설계 및 분석

2018년 7월

서울대학교 대학원

공과대학 화학생물공학부 에너지환경화학융합기술전공

이 대 혁

Abstract

Design and Analysis of Silicon and Titanium Dioxide Anodes for Lithium-ion Batteries

Dae-Hyeok Lee

School of Chemical & Biological Engineering

Chemical Convergence for Energy & Environment

Seoul National University

Lithium-ion batteries (LIBs) are energy conversion/storage devices that convert electrical energy and chemical energy to each other using the chemical potential difference of lithium ions in two electrode materials. Due to high energy density of LIBs, they are used as a power source for many portable devices. As the demand for electric vehicles increases, LIBs are required to have higher performances. Therefore, much research has been conducted to improve performance and the focus of many researchers is to develop electrode materials with higher capacities to achieve higher energy densities. There are several difficulties to use higher specific capacity materials that replace graphite and LiCoO₂, which are currently commercially available electrode materials. In the case of high-capacity alloys or conversion

reaction material, the structural anxiety due to new chemical bonding and volume expansion due to the reaction with many lithium ions are the biggest problem, and studies are under way to secure stability by applying various structures. On the other hand, the insertion reaction materials which are stable in reaction with lithium are undergoing surface modification or nanostructure application in order to achieve additional capacity. The most common of these methods is to enhance the structural stability by applying a porous structure to the electrode material while achieving excellent speed characteristics due to the wider surface area at the same time. Furthermore, it can be expected that the optimized performance can be obtained by designing and applying a porous structure to the characteristics of the electrode material.

In this study, I first tried to apply a porous structure to efficiently use silicon as a lithium ion battery anode. A well-known method for easily obtaining porous silicon is magnesiothermic reaction in which silica is converted into porous silicon by using magnesium reduction power. Experiments have been carried out in view of the fact that magnesium silicide acts as a reaction intermediate in this reaction, and it has been found that Mg_2Si can smoothly reduce oxides of other group IVA elements (CO_2 , GeO_2 , SnO_2) as well as silica. It was confirmed that it is possible to synthesize a complex of porous silicon and another material through this reaction, and this structure helps the stability of silicon. In addition, by using the starting material as the easily obtainable sea sand, the possibility of application in real industry has been opened, and the empty space of the material can be additionally obtained to improve the performance of the silicon/carbon composite.

In the remainder of this study, I have applied a porous structure to overcome the limitations of anatase titanium dioxide. The anatase TiO_2 is theoretically known to react with up to one lithium to exhibit a capacity of 330 mAh g^{-1} . However, when 0.5 lithium in the inner lattice enters the phase transition to lithium titanate, the lithium ion diffusivity rapidly decreases and the reaction does not proceed any more. It is well known, however, that using nanoparticles of sufficiently small size less than 7 nanometers can overcome this kinetic barrier. Therefore, using porous anatase TiO_2 hollow spheres made of nanoparticles having a size 5 nanometers as lithium ion battery electrode materials, it showed high initial capacity such as 330 mAh g^{-1} and excellent long-term performance (195 mAh g^{-1} at 500th cycle) due to its stable structure. The *in-situ* analysis confirmed that the reason for the high capacity is the additional phase transition of individual particle that occurs due to the insertion of lithium ions into the lattice of anatase TiO_2 rather than the commonly known surface reaction.

Contents

Abstract	i
List of Tables	v
List of Figures	vi
Chapter 1. Introduction	
1.1. Lithium-ion batteries (LIBs)	1
1.2. Recent issues on LIBs	7
1.3. Objective of this dissertation	11
1.4. References	13
Chapter 2. Sea sand-derived magnesium silicide as a reactive precursor for silicon-based composite electrodes of lithium-ion battery	
2.1. Introduction	16
2.2. Experimental	21
2.3. Results and discussion	26
2.4. Conclusion	58
2.5. References	59
Chapter 3. Engineering titanium dioxide nanostructures for excess lithium ion storage	
3.1. Introduction	69
3.2. Experimental	71
3.3. Results and discussion	75
3.4. Conclusion	96
3.5. References	97
국문초록	104

List of tables

Table 1.1 Electrochemical performance of nanostructured and bulk anode materials.	10
.....	
Table 2.1 Free energy changes of the reactions between Mg ₂ Si and IVA group oxides.	30
.....	
Table 3.1 Comparison of Li storage performance on recent anatase TiO ₂ nanostructures.	82
.....	

List of Figures

Fig. 1.1 (a) Relative energy diagram of electrode potentials and electrolyte energy gap in LIBs; (b) schematic diagram of the lithium intercalation–de-intercalation reaction mechanism in a rechargeable lithium-ion battery containing solid electrodes and a liquid electrolyte.	3
Fig. 1.2 A schematic representation of the different reaction mechanisms observed in electrode materials for LIBs.	6
Fig. 1.3 (a) Characterization of the main three kinds of EVs: light EV, PHEV and full EV, in terms of performance and battery properties. (b) Ragone plot.	9
Fig. 2.1 (a) XRD patterns after thermal treatment of pristine commercial Mg ₂ Si at 710 °C or 860 °C. (b) Photograph before and after treating the pristine Mg ₂ Si at 860 °C with SiO ₂ located beside.	28
Fig. 2.2 XRD pattern of the crude product obtained from the SiO ₂ located next to Mg ₂ Si after annealing at 860 °C.	29
Fig. 2.3 XRD patterns of (a) solely annealed commercial Mg ₂ Si at 710 °C for 15 h and the as-reacted products between commercial Mg ₂ Si and (b) CO ₂ , (c) SiO ₂ , (d) GeO ₂ , and (e) SnO ₂ at 710 °C for 15 h.	34
Fig. 2.4 Phase diagrams of (a) Si-Ge [2.44] and (b) Si-Sn [2.45]; a red star is marked at the reaction conditions that were used.	35
Fig. 2.5 Raman spectrum of the HCl-treated material for the reaction between Mg ₂ Si and GeO ₂ at 710 °C for 15 h.	36
Fig. 2.6 (a) Synthesis scheme from sea sand to porous Si@C via Mg ₂ Si, (b) XRD patterns of calcined sea sand-derived Mg ₂ Si, and (c) XRD patterns of the as-reacted material from the reaction between sea sand-derived Mg ₂ Si and Na ₂ CO ₃ at 710 °C	

for 5 h with reactant ratios of 1:1.0, 1:0.8, 1:0.6, 1:0.5, and 1:0.4 ($Mg_2Si:Na_2CO_3$)	40
Fig. 2.7 SEM images of sea sand.	41
Fig. 2.8 SEM images of sea sand-derived Mg_2Si	42
Fig. 2.9 XRD patterns of (a) sea sand-derived Mg_2Si annealed at 710 °C for 15 h and (b) mixture of commercial Mg_2Si and Na_2O with a molar ratio of 1:2.0 annealed at 710 °C for 5 h.	43
Fig. 2.10 TGA plot of porous Si@C-0.6 produced with a sea sand-derived $Mg_2Si:Na_2CO_3$ ratio of 1:0.6.	44
Fig. 2.11 (a) XRD patterns of as-reacted and HCl-treated products from the reaction between commercial Si and Na_2CO_3 (1:1 mole ratio) at 710 °C for 3 h and (b) IR spectra of commercial Si, as-reacted product, and HCl-treated products from the reaction between commercial Si and Na_2CO_3 at 710 °C for 3 h.	45
Fig. 2.12 (a) XRD pattern, (b) TGA plot, (c) Raman spectrum, (d) SEM image, (e) TEM image, (f) TEM-EDX Si map, (g) TEM-EDX C map, (h) HR-TEM image, and (i) SAED pattern of HCl- and HF-treated materials from the reaction between the sea sand-derived Mg_2Si and Na_2CO_3 with a ratio of 1:1 at 710 °C 5 h (porous Si@C-1).	49
Fig. 2.13 SEM image of acid-treated products from the reaction between commercial Si and Na_2CO_3 (1:1 mole ratio) at 710 °C for 5 h; it can be clearly seen that porous Si is encapsulated in a carbon shell.	50
Fig. 2.14 (a, b) TEM images of as-reacted material from the sea sand-derived Mg_2Si and Na_2CO_3	51
Fig. 2.15 (a) Cycling performance of porous Si@C-0.6 and porous Si@C-1	

synthesized with Mg ₂ Si:Na ₂ CO ₃ ratios of 1:0.6 and 1:1. Voltage profiles of (b) porous Si@C-0.6 and (c) porous Si@C-1 extracted from the cycling performance test at 0.4 A/g.	55
Fig. 2.16 Rate capability of porous Si@C-1.	56
Fig. 2.17 (a) Schematic of the preparation of porous Si@Ge that employs Mg ₂ Si as a reactive Si source and GeO ₂ , (b) XRD pattern, (c) SEM image of central region (inset: low-magnification image), and (d-e) SEM-EDX mapping data of porous Si@Ge, (f) cycling performance of porous Si@Ge at a current density of 0.4 A/g, and (g) rate performance of porous Si@Ge.	57
Fig. 3.1 Schematic illustration of size selection of constituent nanocrystals in (A) 5 HT and (B) 12 HT.	73
Fig. 3.2 Schematic illustration on engineering TiO ₂ nanostructures for excess Li ion storage.	74
Fig. 3.3 Representative TEM images of the prepared hollow anatase TiO ₂ nanostructures. Low magnification TEM images of (A) 5 HT and (B) 12 HT (scale bar = 100 nm). The insets in A and B are the selected area electron diffraction patterns, which confirm the anatase structures of 5 HT and 12 HT. High magnification TEM images of (C) 5 HT and (D) 12 HT (scale bar = 20 nm).	76
Fig. 3.4 XRD patterns of prepared anatase TiO ₂ nanomaterials (5 HT, 12 HT, 5 NC and 15 NC).	77
Fig. 3.5 Representative TEM images of (A) 5 NC and (B) 15 NC.	78
Fig. 3.6 Electrochemical measurements on the prepared anatase TiO ₂ anodes. A) Cycling performance of the anatase TiO ₂ nanomaterials at 0.1 A g ⁻¹ (5 HT, 12 HT, 5 NC, and 12 NC). B) Cycling performance of 5 HT at different charge-discharge rates (0.1–5 A g ⁻¹). C) Voltage profiles of 5 HT and 12 HT during the first discharge. D)	

Capacity and ratio of three regions in 5 HT during 500 cycles. E) Long-life cycling performance of 5 HT at 0.1 A g^{-1}	81
Fig. 3.7 Voltage profiles of 5 HT for various cycle number.	86
Fig. 3.8 Representative TEM images of 5 HT in (A) low and (B) high magnification after the first lithium charging.	84
Fig. 3.9 High-resolution TEM images of 5 HT indicating thin solid-electrolyte interphase (SEI) layer formation after the first lithium charging.	85
Fig. 3.10 Representative TEM images of 5 HT in (A) low and (B) high magnification after 200 cycles.	86
Fig. 3.11 Voltage profiles of (A) 5 NC and (B) 15 NC during the first discharge. ..	97
Fig. 3.12 Characterization by <i>in-situ</i> XRD. A) Voltage profiles of 5 HT and 12 HT in the first cycle. B) Series of <i>in-situ</i> XRD data for the charge-discharge process of 5 HT in the first cycle. C) Series of <i>in-situ</i> XRD data for the charge-discharge process of 12 HT in the first cycle. D) Corresponding d-values of the (101) planes (for TiO_2 and LiTiO_2) and the (011) plane (for $\text{Li}_{0.55}\text{TiO}_2$) obtained from the <i>in-situ</i> XRD results.	90
Fig. 3.13 Crystal structures of anatase TiO_2 during lithium intercalation. Each structures indicate (A) anatase, (B) lithium titanate and (C) LiTiO_2	91
Fig. 3.14 <i>in-situ</i> XRD measurement of 5 HT in 21 st cycle. Similar to Fig.3.12B, sequential phase transition can be observed on constituent crystals in 5 HT from anatase to LiTiO_2 through lithium titanate in 21 st cycle.	92
Fig. 3.15 <i>in operando</i> GITT measurement at the 1 st discharge on 5 HT and 12 HT. GITT method was carried out with 4 mA g^{-1} for 1 hour and rest for 2 hour.	93

Fig. 3.16 Characterization by *in-situ* XAS. A, B) *in-situ* Ti K-edge XANES data recorded on the first discharge of 5 HT. The inset in A) is the change in the edge position during lithium intercalation. 95

1. Introduction

1.1. Lithium-ion batteries (LIBs)

Lithium-ion batteries are energy storage devices that reversibly switch between chemical and electrical energy, storing and releasing energy through the difference in lithium ion potential between the two electrodes. At this time, lithium ion, which is a medium for transferring energy, reversibly reacts with the two electrode materials to cause an oxidation / reduction reaction. The relationship between the chemical energy and the electric energy inside the lithium ion battery is expressed by the following equation:

$$\Delta G_{cell} = \mu_{cathode} - \mu_{anode} = -nF(E_{cathode} - E_{anode}) = -nFE_{cell}$$

As can be seen from the above equation, lithium ions have higher chemical potential at the anode than at the cathode, so they emit energy through a spontaneous movement from the anode to the cathode, which is transferred in the form of current through an external circuit. During this time, the cathode material is reduced and the anode material is oxidized, so that the potential difference between the two electrodes gradually decreases, which is called discharge. In order to store energy in the LIB, an external work is performed to cause a reaction in the opposite direction to increase the potential difference between the two electrodes, which is called charging.

The key components of the LIB are electrode material, electrolyte and separator. The electrode material is used as an anode and a cathode according to the reaction

potential with lithium. The role of the electrolyte is to transport lithium ions between the two electrodes, which consists of a salt containing lithium ions and a solvent that can dissolve it. Electrolyte components should not cause any electrical reaction other than lithium ion. Therefore, stable organic anions such as PF_6^- , and electrically stable carbonate-based organic materials having a high dielectric constant to dissolve salts are mainly used. The separator physically separates the two electrodes so that they do not come into contact. The membrane needs to be well wetted with electrolyte and to transfer lithium ions well. However, if a short circuit occurs between the two electrodes due to a problem in the separation membrane, safety problems such as explosion may occur. Therefore, the most important property of the separation membrane is thermal stability. Polyolefin materials such as PE and PP are mainly processed into porous membranes and used as membranes.

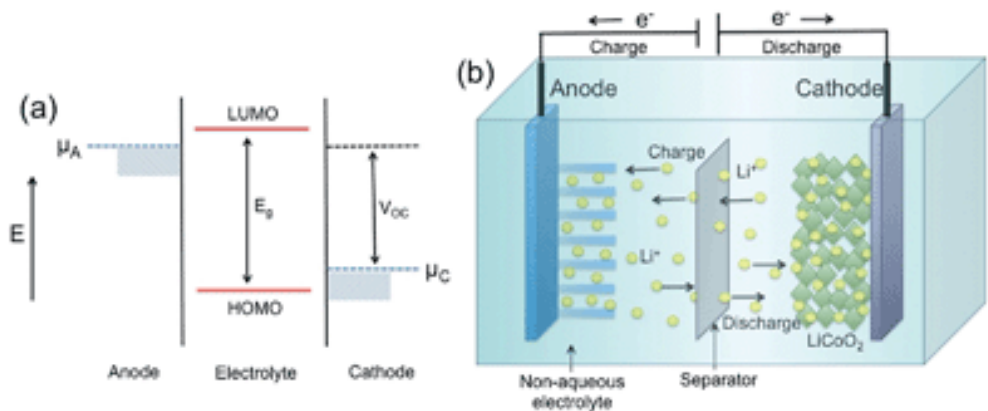


Fig. 1.1 (a) Relative energy diagram of electrode potentials and electrolyte energy gap in LIBs; (b) schematic diagram of the lithium intercalation–de-intercalation reaction mechanism in a rechargeable lithium-ion battery containing solid electrodes and a liquid electrolyte. Adapted from Ref. [1.1]

Electrode materials can be divided into three types, conversion, alloying, and intercalation, depending on the method of storing lithium ions, except when using lithium metal directly. First, the intercalation material stores lithium ions through a reaction in which lithium ions are intercalated/deintercalated into a metal oxide lattice containing or not containing lithium. The structural stability of the material is excellent and the potential is not changed according to the reaction of lithium, so that the reaction voltage has plateau, but the capacity is generally low. Representative materials are graphite, LiCoO_2 , and TiO_2 . The second is the alloying material that stores lithium ions through a reversible alloy reaction with lithium. It has a relatively large capacity because it can react with several lithium atoms per atom of the host material, but it has a disadvantage in that stability is deteriorated due to a large volume change and physical property change due to the alloy reaction with lithium. Representative materials are Si, Ge, and Sn. The third is the conversion material, which is a metal oxide or sulfide material that stores lithium ions through reversible reaction to form lithium oxide or lithium sulfide. Although it has the advantage that it can express large capacity according to the number of oxygen or sulfur atom, it has a disadvantage of wide range of reaction voltage and having large hysteresis. Representative materials are iron oxide and cobalt sulfide. [1.2]

LIB, which is currently commercialized, was developed by SONY using graphite anode and LiCoO_2 cathode developed in the 1980s. [1.3, 1.4] Since they are layered materials with an intercalation mechanism, they both have a stable charge/discharge voltage and have higher energy density than other rechargeable batteries (Ni-Cd and lead-acid batteries). In addition, it is widely used in mobile devices because it is easy

to manufacture in various forms and there are few other problems such as self-discharge and memory effect.

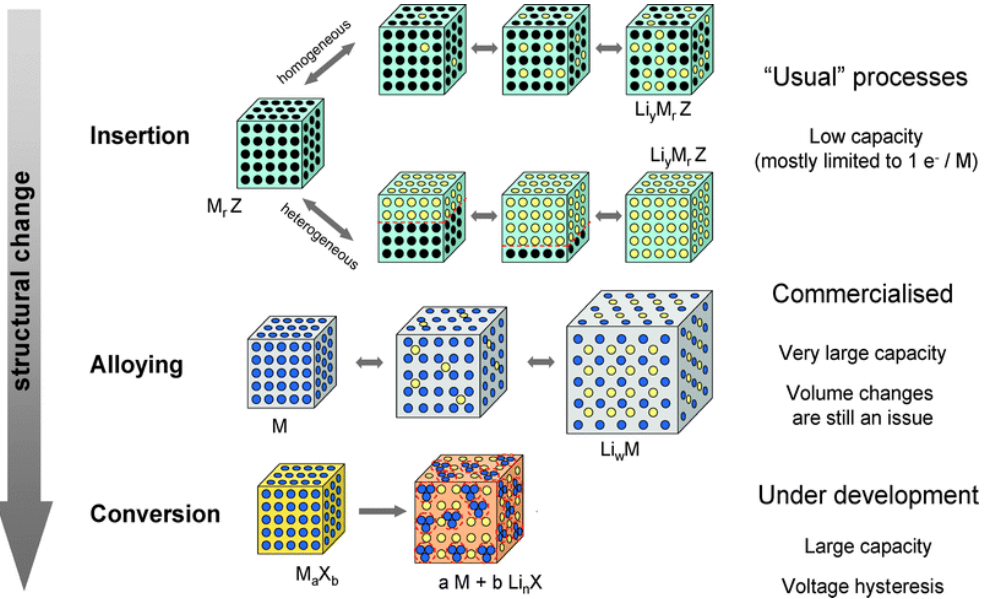


Fig. 1.2 A schematic representation of the different reaction mechanisms observed in electrode materials for LIBs. Adapted from Ref. [1.2]

1.2. Recent issues on LIBs

Lithium-ion batteries are the most notable energy storage and conversion devices in recent years and have many applications. Especially, electric vehicle (EV) and energy storage system (ESS) that show explosive growth require higher performance than currently used LIBs, so various researches are being conducted to enhance the performance. Among them, energy density is the highest priority, and energy density can be improved by increasing unit capacity and driving voltage. Generally, it is considered difficult to increase the driving voltage of the battery because the reaction voltage with lithium is the intrinsic property of the electrode material. Some researchers have attempted to secure additional high-voltage capacity through some methods such as doping for some cathode materials. [1.5]

The electrode material with the intercalation mechanism has a low capacity since lithium ions can only enter a limited part of the inner lattice in host material. To overcome this, using amorphous materials with lower crystallinity (e.g. hard carbon, a-TiO₂) can increase the capacity because additional lithium can be stored at the defect location. [1.6, 1.7] However, in this case, the coulomb efficiency decreases and the reaction voltage range is widened. Conversion or an alloying mechanism is expected to be a new electrode material of LIBs because it has a large capacity of more than 1,000 mAh g⁻¹. [1.8–1.10] For these materials, since particles are frequently broken because of large volume expansion due to a large unit capacity, a method of securing a buffer space by applying a nanostructure can be effectively applied. [1.11] Also, reducing the diffusion distance of lithium ions through

nanostructures can overcome the limitation of slower kinetic because of the need to create new bonds. In order to solve these problems mentioned above, it is known that coating an additional carbon material is also effective. [1.12] Carbon coating is the most commonly tried method because it can maintain the structure of the material and improve the electron conductivity.

Power density as well as energy density are also important in applications where higher power is required. Among the methods mentioned above, applying nanostructure or using carbon coating can also be applied to increase power density because it improves the kinetic property of electrode materials. In addition, methods of doping or amorphizing the surface to promote the charge transfer reaction on the surface have been studied. [1.13, 1.14] The lithium ion diffusion in the electrolyte as well as the electrode material plays an important role in the power density, so it is also a major strategy to smooth it by designing the electrode material mesoporously. [1.15, 1.16]

a Modes of operation	battery capacity needed, kWh	Energy density, Wh/kg	Weight of battery, Kg	Speed, kilometres per hour	Distance on one charge, kilometres
Hybrid	<3	40-50 (Ni-MH)	60 (Ni-MH)	100+	15
Plug in Hybrid	5.6-18	90-100 (Li-ion)	60-200 (Li-ion)	100+	10-60
Full EV	35-54	90-100 (Li-ion)	450 (Li-ion)	>100	150-200

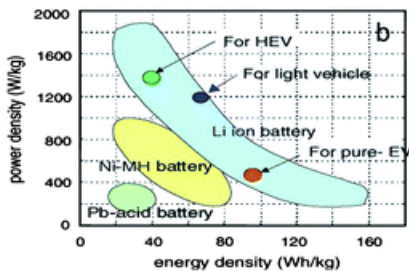


Fig. 1.3 (a) Characterization of the main three kinds of EVs: light EV, PHEV and full EV, in terms of performance and battery properties. (b) Ragone plot. Adapted from Ref. [1.17]

Table 1.1 Electrochemical performance of nanostructured and bulk anode materials.

Adapted from Ref. [1.11]

Anode materials	Capacity (mAh g ⁻¹)		Current density	Voltage (V)
	Initial	After <i>n</i> th cycle		
Silicon bulk particles	~3,260	~200 (10th)	100 mA/g	2.0–0.0
3D porous silicon	~3,138	~2,800 (100th)	400 mA/g	1.5–0.0
Silicon nanotubes	~3,200	~3,000 (80th)	3,000 mA/g	1.5–0.0
Silicon nanowires	~4,200	~3,300 (10th)	210 mA/g	2.0–0.01
SiO _x /C on Si NP	~2,200	~1,100 (60th)	150 mA/g	1.0–0.05
Si/CNT film	~2,400	~1,600 (50th)	360 mA/g	1.0–0.01
Co ₃ O ₄ bulk particles	~1,200	~80 (20th)	111 mA/g	3.0–0.0
Co ₃ O ₄ nanoparticles	~1,230	~200 (60th)	100 mA/g	3.0–0.005
Co ₃ O ₄ nanowires	~1,300	~200 (60th)	100 mA/g	3.0–0.005
Mesoporous Co ₃ O ₄	~1,330	~820 (60th)	100 mA/g	3.0–0.005
Self-supported Co ₃ O ₄ nanowires	~1,124	~700 (20th)	111 mA/g	3.0–0.0
Non-supported Co ₃ O ₄ nanowires	~1,124	~350 (20th)	111 mA/g	3.0–0.0
CuO (1 μm)	~400	~380 (70th)	0.2 C	3.0–0.02
CuO (0.15 μm)	~410	~100 (70th)	0.2 C	3.0–0.02
CuO urchin structure	~800	~560 (50th)	150 mA/g	3.0–0.001
CuO hollow cubes	~967	~79 (50th)	150 mA/g	3.0–0.001
CuO hollow spheres	~900	~91 (50th)	150 mA/g	3.0–0.001
SnS ₂ bulk particles	~401	~127 (30th)	50 mA/g	3.0–0.0
SnS ₂ nanoplates	~1,311	~583 (30th)	323 mA/g	1.1–0.001
SnS ₂ nanoflowers	~1,650	~502 (50th)	200 mA/g	1.2–0.05

1.3. Objective of this dissertation

Through this study, I tried to improve the performance by applying the porous structure to two different electrode materials. First, the improved performance was obtained by the porous Si/C structure applying the new chemical reaction inspired from magnesiothermic reaction. Secondly, the nano-crystalline anatase TiO₂ with the mesoporous hollow sphere structure was synthesized and analyzed to reveal the cause of the performance improvement through several *in-situ* analysis.

Silicon is a typical alloying mechanism electrode material that reacts with up to 4.4 lithium atoms per atom and exhibits a capacity of 4,200 mAh g⁻¹. Many of the methods for solving large volume expansion have been attempted. Especially, reduction of SiO₂ by magnesiothermic reaction using reducing power of magnesium is attracting attention as a simple method of making mesoporous silicon. In the first step of this reaction, excess Mg reacts with SiO₂ to form Mg₂Si, and in the second step, this Mg₂Si reacts with SiO₂ to form mesoporous silicon. Noting this second step, we have confirmed that reacting Mg₂Si with oxide materials of Group IVA (C, Si, Ge and Sn) can produce a composite material. The mesoporous Si/C was produced by reacting Na₂CO₃ and Mg₂Si produced from sea sand and applied to LIB anode to obtain high performance of 1000 mAh g⁻¹ was obtained in 200 cycles. The use of this modified magnesiothermic reaction is a key part of the first part, that a well-designed mesoporous silicon composite can be made.

In the second part, mesoporous anatase TiO₂ with a hollow sphere structure was synthesized by a simple method. When this material was applied to the LIB anode,

its performance was improved and its origins were confirmed using various *in-situ* analytical methods. Anatase TiO₂ is an insertion mechanism electrode material and has high stability. However, in general, only about half of the theoretical capacity of 330 mAh g⁻¹ can be used. This is because lithium titanate (Li_{0.5}TiO₂) phase generated by lithium insertion does not have sufficient lithium ion diffusivity, and the next phase transition does not occur. It is well known that particles smaller than 7 nm can proceed to the LiTiO₂ phase beyond this kinetic barrier, but this is rarely observed directly in a typical driving environment. The mesoporous anatase TiO₂ used in this study with individual particles with a size of about 5 nm in the form of a hollow sphere exhibited a capacity of 228 mAh g⁻¹ in 100 cycles. In order to clarify the cause of these improved capacities, *in-situ* XRD and XAFS analysis actually confirmed the transition to LiTiO₂ phase. This is the result of knowing that the electrode material can perform well beyond the limits known to be kinetically inhibited when it is well designed with nanostructure.

1.4. References

- [1.1] Roy, P. and S. K. Srivastava, "Nanostructured anode materials for lithium ion batteries", *Journal of Materials Chemistry A*, **2015**, *3*, 2454.
- [1.2] Palacin, M. R., "Recent advances in rechargeable battery materials: a chemist's perspective", *Chemical Society Reviews*, **2009**, *38*, 2565.
- [1.3] Yazami, R. and P. Touzain, "A reversible graphite-lithium negative electrode for electrochemical generators", *Journal of Power Sources*, **1983**, *9*, 365.
- [1.4] Mizushima, K., P. C. Jones, P. J. Wiseman and J. B. Goodenough, "Li_xCoO₂ (0 < x < -1): A new cathode material for batteries of high energy density", *Materials Research Bulletin*, **1980**, *15*, 783.
- [1.5] Hu, M., X. Pang and Z. Zhou, "Recent progress in high-voltage lithium ion batteries", *Journal of Power Sources*, **2013**, *237*, 229.
- [1.6] Buiel, E. and J. R. Dahn, "Li-insertion in hard carbon anode materials for Li-ion batteries", *Electrochimica Acta*, **1999**, *45*, 121.
- [1.7] Lin, Y.-M., P. R. Abel, D. W. Flaherty, J. Wu, K. J. Stevenson, A. Heller and C. B. Mullins, "Morphology Dependence of the Lithium Storage Capability and Rate Performance of Amorphous TiO₂ Electrodes", *The Journal of Physical Chemistry C*, **2011**, *115*, 2585.

[1.8] Koo, B., H. Xiong, M. D. Slater, V. B. Prakapenka, M. Balasubramanian, P. Podsiadlo, C. S. Johnson, T. Rajh and E. V. Shevchenko, "Hollow Iron Oxide Nanoparticles for Application in Lithium Ion Batteries", *Nano Letters*, **2012**, *12*, 2429.

[1.9] Chan, C. K., H. Peng, G. Liu, K. McIlwrath, X. F. Zhang, R. A. Huggins and Y. Cui, "High-performance lithium battery anodes using silicon nanowires", *Nature Nanotechnology*, **2007**, *3*, 31.

[1.10] Nam, K. T., D.-W. Kim, P. J. Yoo, C.-Y. Chiang, N. Meethong, P. T. Hammond, Y.-M. Chiang and A. M. Belcher, "Virus-Enabled Synthesis and Assembly of Nanowires for Lithium Ion Battery Electrodes", *Science*, **2006**, *312*, 885.

[1.11] Song, M.-K., S. Park, F. M. Alamgir, J. Cho and M. Liu, "Nanostructured electrodes for lithium-ion and lithium-air batteries: the latest developments, challenges, and perspectives", *Materials Science and Engineering: R: Reports*, **2011**, *72*, 203.

[1.12] Goriparti, S., E. Miele, F. De Angelis, E. Di Fabrizio, R. Proietti Zaccaria and C. Capiglia, "Review on recent progress of nanostructured anode materials for Li-ion batteries", *Journal of Power Sources*, **2014**, *257*, 421.

[1.13] Ma, Y., B. Ding, G. Ji and J. Y. Lee, "Carbon-Encapsulated F-Doped $\text{Li}_4\text{Ti}_5\text{O}_{12}$ as a High Rate Anode Material for Li^+ Batteries", *ACS Nano*, **2013**, *7*,

10870.

[1.14] Xia, T., W. Zhang, J. Murowchick, G. Liu and X. Chen, "Built-in Electric Field-Assisted Surface-Amorphized Nanocrystals for High-Rate Lithium-Ion Battery", *Nano Letters*, **2013**, *13*, 5289.

[1.15] Chen, H., Q. Zhang, J. Wang, D. Xu, X. Li, Y. Yang and K. Zhang, "Improved lithium ion battery performance by mesoporous Co₃O₄ nanosheets grown on self-standing NiSix nanowires on nickel foam", *Journal of Materials Chemistry A*, **2014**, *2*, 8483.

[1.16] Jin, J., S.-Z. Huang, J. Liu, Y. Li, D.-S. Chen, H.-E. Wang, Y. Yu, L.-H. Chen and B.-L. Su, "Design of new anode materials based on hierarchical, three dimensional ordered macro-mesoporous TiO₂ for high performance lithium ion batteries", *Journal of Materials Chemistry A*, **2014**, *2*, 9699.

[1.17] Etacheri, V., R. Marom, R. Elazari, G. Salitra and D. Aurbach, "Challenges in the development of advanced Li-ion batteries: a review", *Energy & Environmental Science*, **2011**, *4*, 3243.

2. Sea sand-derived magnesium silicide as a reactive precursor for silicon-based composite electrodes of lithium-ion battery

2.1. Introduction

Over the past decades, Si-based anode materials have been a matter of primary concern for researchers investigating Li-ion batteries. This is because Si-based anode materials are considered to be the most promising substitutes for conventional carbon-based anodes because of the high theoretical capacity of Si ($\sim 4200 \text{ mAh g}^{-1}$) [2.1]. However, there are notorious obstacles that must be overcome in order to utilize Si as an anode material. For example, its volume expansion and low electrical conductivity result in unstable cycling performance and low rate capability, respectively [2.2–2.4]. In addition, the continuous formation of a solid-electrolyte interphase (SEI) layer upon cycling retards Si utilization and causes poor cycling performance [2.4, 2.5]. Accordingly, many researchers have investigated these problems.

Three important lessons have been derived from these research. First, Si-based anode materials should possess an appropriate architecture that can accommodate the volume expansion of Si. For instance, Si in the form of nanowires [2.6], hollow nanoparticles [2.7], porous Si [2.8], and Si encapsulated in the void space of a protective framework are known to be effective [2.9–2.11]. Second, Si should be

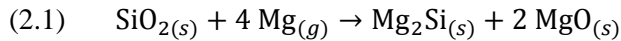
hybridized with conductive materials to overcome the low intrinsic electronic conductivity of Si. Carbonaceous materials have typically been used as this component [2.12–2.16], but other materials, including Ag [2.17, 2.18], Ge [2.19, 2.20], and TiSi₂, have also been reported. [2.21]. Hybridizing materials with Si can enhance the electron transferring efficiency to Si, thereby improving the rate capability of Si-based anode materials. Third, depletion of the electrolyte through SEI formation can be alleviated by forming SEI layers on the surface of carbon shells that contain the Si active materials [2.5].

The desired structure of Si-based anode materials is clear; hence, the remaining issues are related to synthesizing Si-based anode materials by using approaches that can be combined with industrial applications. Common methods that have been utilized in the literature to prepare nanostructured Si are chemical vapor deposition (CVD) of Si precursors (e.g., SiH₄) or metal-assisted etching and electrochemical anodization of Si wafers [2.22–2.25]. These approaches can be used to prepare nanostructured Si materials with excellent electrochemical performance. However, they are costly, small-scale, and environmentally-unfriendly processes using explosive silane precursor and hazardous hydrofluoric (HF) acid. Also, additional steps are required to encapsulate the nanostructured Si in conductive and protective materials. Therefore, these approaches are not appropriate for the mass production of Si-based electrodes.

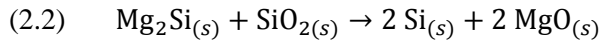
Among other approaches, magnesiothermic reduction, which produces Si by reducing SiO₂ with magnesium (Mg), has attracted attention [2.26–2.30]. This

technique is appealing because it can adopt naturally-abundant SiO₂ sources, such as rice husks [2.31, 2.32], sands [2.33, 2.34], reed plants [2.35], and clay, as Si sources [2.36]. In addition, it can be performed on a large scale without specialized reaction equipment because the reactants are all in a solid state; accordingly, it is a facile, cost-effective, and sustainable synthetic method that can be used to prepare Si-based anode materials.

Motivated from the advantages of magnesiothermic reduction, considerable efforts have been devoted to elucidate the reaction mechanism of magnesiothermic reduction. It was determined that magnesium silicide (Mg₂Si) is *in-situ* formed when Mg is used, as described in reaction (2.1) [2.33, 2.37].



Subsequently, Mg₂Si reacts with the remaining SiO₂, and thereby Si is formed, as described in reaction (2.2) [2.33, 2.37].



Interestingly, reaction (2.2) shows that Mg₂Si still possesses sufficiently high reactivity to reduce SiO₂, despite the fact that SiO₂ is a highly-stable oxide. The powerful reactivity of Mg₂Si enough to reduce SiO₂ can be attributed to the binding nature between Mg and Si. As revealed by X-ray photoelectron spectroscopy (XPS), the ionic bonding character between Mg and Si is only 9%, implying that the Mg in Mg₂Si still tends to react with other compounds to donate their electrons [2.38]. The high reactivity of Mg₂Si has recently been reported by Ahn et al.; the Mg₂Si

intermediate that is *in-situ* formed during magnesiothermic reduction can react with carbon to produce SiC at moderate temperatures (600–750 °C), where the direct reaction between Si and carbon hardly occurs [2.39, 2.40]. Also, the Qian group has demonstrated that such Mg₂Si or Mg₂Ge compounds possess sufficient reactivity to reduce Ge⁴⁺ or Sn²⁺ ion, respectively [2.41, 2.42]. In addition, it is worth mentioning that Mg is the predominant diffusion species in Mg₂Si when it is annealed at temperatures over 275 °C [2.43]. Thus, the mobility of Mg in Mg₂Si enables reaction (2.2) to be completed, despite the fact that the reactants are in solid states.

Inspired by reaction (2.2), we could assume that Mg₂Si would reduce adequately chosen oxides (instead of SiO₂), resulting in a composite of Si from Mg₂Si and reduced material of a chosen oxide. Based on this assumption, in this research, we investigated utilization of Mg₂Si serving as a reactive precursor for Si-based composites. Reactivity of Mg₂Si to oxides was confirmed using commercial Mg₂Si (made from the reaction of Si and Mg). A variety of group IVA oxides (CO₂, SiO₂, GeO₂, and SnO₂) as the counter reactants was tested, and thereby it was found that Mg₂Si readily reacts with the solid oxides (SiO₂, GeO₂, and SnO₂), with the exception of CO₂ (presumably due to its gaseous nature). These reactions result in Si with reduced forms of the counter oxides (i.e., Si, Ge, and Sn), so Si-based composites with Ge, and Sn composites were successfully prepared when GeO₂ or SnO₂ was utilized as a counter reactant instead of SiO₂. Interestingly, it was also found that consumption of Mg in Mg₂Si by the reaction induces macroporosity of Si which is a desirable structural feature of Si-based anode. Accordingly, it can be concluded that a simple solid-state reaction using Mg₂Si as a reactive precursor can

be utilized to produce nanostructured Si-based composites without aforementioned hazardous, costly, and environmentally-unfriendly synthetic methods.

In later part, we focused on developing a more practically and electrochemically attractive material, porous Si@C, based on the reaction of Mg₂Si. Notably, sea sand-derived Mg₂Si was adopted instead of commercial Mg₂Si. This confirmed that this modified magnesiothermic reaction also possesses advantages of adopting naturally abundant sources, making the process more sustainable, economic, and scalable. In order to realize composite of Si and C which is more electrochemically attractive, carbonate (a solid form of CO₂) was utilized as a counter oxide. The Mg₂Si derived from sea sand successfully transformed Na₂CO₃ to carbon at the surface; hence, porous Si encapsulated in a carbon shell (porous Si@C) was obtained. Detailed synthetic approaches for realizing an ideal Si@C composite, as well as the fundamentals for the solid-state reaction of this modified magnesiothermic reduction, are studied. Lastly, prepared porous Si@C from sea sand and the modified magnesiothermic reduction was tested as anodes for LIBs, showing a reversible capacity of nearly 1,000 mAh/g (even at the 200th cycle) at a rate of 0.4 A/g.

2.2. Experimental

2.2.1. Materials

Mg_2Si (> 99%, 20 mesh), SnO_2 nanopowder (< 100 nm), Na_2CO_3 (> 99.5%), Ge ethoxide (99.95%), and Na_2O (80%) were purchased from Sigma-Aldrich. Na_2CO_3 was dried under reduced pressure at 100 °C before use. GeO_2 (99.9999%) was purchased from Wako Pure Chemical Industries (Japan). Magnesium (Mg, 325 mesh) and commercial Si nanoparticles (~100 nm) were purchased from Alfa-Aesar. Sea sand was purchased from Yakuri Pure Chemicals (Japan). Hydrochloric acid (HCl, 35-36%) was purchased from Samchun Chemical (Korea). Hydrofluoric acid (HF, 48-51%) was purchased from JT Baker. Deionized (DI) water, purified with a Milli-Q purification system, was used for all experiments

2.2.2. Lability Confirmation of Mg_2Si under Thermal Treatment

228 mg (3 mmol) of Mg_2Si was placed in an alumina crucible and annealed at 710 °C or 860 °C for 15 h with a ramping rate of 10 °C/min in a horizontal tube furnace under an Ar gas flow. In addition, while attempting to confirm the formation of Mg gas from Mg_2Si , SiO_2 was located beside the Mg_2Si with an iron mesh separator.

2.2.3. Reaction between Mg_2Si and Oxides

For the solid state oxide materials, 228 mg (3 mmol) of Mg_2Si was mixed with the counter reactant (SiO_2 , GeO_2 , and SnO_2). The amount of oxide was selected such that the mole ratio between Mg and O was 1:1. This mixture was placed in an

alumina crucible and annealed at 710 °C for 15 h with a ramping rate of 10 °C/min in a horizontal tube furnace under an Ar gas flow. When CO₂ was used as the counter reactant, only Mg₂Si (228 mg) was placed in the crucible and CO₂ was employed as the flow gas instead of Ar.

2.2.4. Synthesis of Sea Sand-Derived Mg₂Si

The purchased sea sand was first calcined at 950 °C for 5 h in a muffle furnace. The calcined product was ground by mortar and pestle and then sieved with a 500 mesh iron sieve. The sieved product was then used to prepare Mg₂Si. Mg was first placed in an alumina crucible and then the sieved sea sand was put on the magnesium. A 500 mesh iron mesh was placed between the magnesium and sea sand to prevent mixing. After the alumina crucible was covered by another alumina crucible, the materials were annealed at 710 °C for 5 h with a ramping rate of 5 °C/min in a horizontal tube furnace under an Ar flow. The product was used for subsequent reactions without any other post-treatments.

2.2.5. Reaction between Sea Sand-Derived Mg₂Si and Na₂CO₃

The sea sand-derived Mg₂Si was mixed with Na₂CO₃ by mortar and pestle with the given mole ratio of Mg₂Si:Na₂CO₃ (1:1.0 to 1:0.4). The amount of Mg₂Si in the sea sand-derived Mg₂Si was determined based upon the assumption that the conversion of sea sand is stoichiometrically completed. The mixture was annealed at 710 °C for 5 h with a ramping rate of 10 °C/min in a horizontal tube furnace under an Ar flow. The crude product was immersed in a 1 M HCl solution to remove by-products and then washed by centrifugation. To leach out the remaining silica, 2 wt%

of an HF aqueous solution was also used. After purification by centrifugation, the product was dried at 100 °C under reduced pressure.

2.2.6. Annealing of the Sea Sand-Derived Mg₂Si

200 mg of the sea sand-derived Mg₂Si was placed in an alumina crucible. This was annealed at 710 °C for 5 h with a ramping rate of 10 °C/min in a horizontal tube furnace under an Ar flow.

2.2.7. Reaction between Commercial Mg₂Si and Na₂O

Commercial Mg₂Si and Na₂O were mixed by grinding. The mole ratio was 1.0:2.0. The mixture was annealed at 710 °C for 5 h with a ramping rate of 10 °C/min in a horizontal tube furnace under an Ar flow.

2.2.8. Reaction between Commercial Si and Na₂CO₃

Commercial Si and Na₂CO₃ were ground together at a mole ratio of 1:1. The mixture was annealed at 710 °C for 3 h with a ramping rate of 10 °C/min in a horizontal tube furnace under an Ar flow. The crude product and the HCl-treated product were analyzed by FT-IR and XRD.

2.2.9. Inductively Coupled Plasma (ICP) Analysis to Reveal the Loss of Na₂O

Two samples were prepared and compared. The first one was the reactant mixture of commercial Mg₂Si and Na₂CO₃ with a mole ratio of 1.0:1.0. The other sample was the product of the first sample annealed at 710 °C for 5 h with a ramping rate of 10 °C/min. Samples were pre-treated with 1 M HCl in order to dissolve all of the Na

and Mg components (e.g., Mg₂Si, MgO, Na₂O, and Na₂CO₃) before the ICP measurements, and the filtered solution was analyzed by ICP. As a result, the relative ratio of Na and Mg could be obtained.

2.2.10. Synthesis of Porous Si@Ge

2.5 mmol of Mg₂Si (191.8 mg) was mixed in 2 mmol of Ge ethoxide (0.504 mg). 0.2 ml of an ammonia solution was injected into the mixture under vigorous stirring. The product gel was entirely dried by heating at 120 °C for at least 16 h. The mixture was placed in an alumina crucible and annealed in a horizontal tube furnace. The temperature was ramped to 710 °C over 2 h and then maintained for 15 h under continuous Ar flow. After annealing, the product was immersed in 1 M HCl for at least 12 h and then dried under vacuum.

2.2.11. Battery Test

The electrochemical performance was evaluated using a CR2032-type coin cell. The prepared samples were used as the cathode, Li metal foil was used as the anode, a 1.0 M LiPF₆ solution in ethylene carbonate (EC)/diethyl carbonate (DEC)/fluoroethylene carbonate (FEC) (5:70:25 vol%, Panatech, Korea) was used as the electrolyte, and a polypropylene membrane (SK innovation, Korea) was used as a separator. The electrode was fabricated by making a slurry composed of the active materials (70 wt%), Super P (10 wt%; as a conducting agent), and polyamideimide (PAI) dispersed in N-methyl-2-pyrrolidinone (NMP, Aldrich) (20 wt%; as a binder). This was coated onto a copper foil using the doctor blade method. The Li coin cells were assembled in an argon-filled glove box. The electrochemical

performance of all of the samples was demonstrated using a WBCS 3000 battery cycler system (WonATech Corp., Korea) in a voltage range of 0.01-1.2 V (versus Li/Li⁺) at 25 °C in an incubator.

2.2.12. Characterization

Normal transmission electron microscope (TEM) images were acquired by a Hitachi-7600 system (Hitachi, Japan). Scanning electron microscope (SEM) images were acquired by a Hitachi S-4300 system (Hitachi, Japan). X-ray fluorescence (XRF) spectroscopy was conducted with an XRF-1800 (Shimadzu, Japan) with samples in a KBr pellet. High-resolution TEM (HR-TEM) images were obtained with a JEM-2100F (JEOL). The thermogravimetric analysis (TGA) was performed using an SDT Q600 device (TA Instruments Inc.) and XRD measurements were performed with a D8 Advance (Bruker) with Cu radiation ($\lambda = 1.5406 \text{ \AA}$) at 40 kV and 40 mA. Elemental analysis was performed by a Flash EA 1112 (Thermo Electron Corp.). Inductively coupled plasma (ICP) analysis was performed by an ICP-730ES (VARIAN). The Raman spectrum was obtained by a T64000 (HORIBA)

2.3. Results and discussion

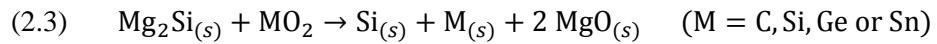
2.3.1. Chemistry of Mg₂Si

First of all, the lability of Mg₂Si during thermal treatment was explored. Pristine commercial Mg₂Si was placed in an alumina crucible and then annealed in a tube furnace under an Ar atmosphere at 710 °C and 860 °C. The resultant products were analyzed by X-ray diffractometer (XRD), as depicted in Fig. 2.1a.

Mg₂Si almost retained its original state after being annealed at 710 °C; only a small amount of Si was formed. However, when annealed at 860 °C, only Si was observed in the final product. This implies that Mg₂Si undergoes thermal decomposition by which labile Mg is released in the gaseous phase, when the temperature is high enough. In an attempt to confirm the formation of gaseous Mg, an experiment was designed as presented in Fig. 2.1b. An iron mesh was placed in between Mg₂Si and SiO₂ and they were annealed at 860 °C. It was verified that SiO₂ was converted into Si and MgO after the heat treatment, implying the development of gaseous Mg from Mg₂Si at 860 °C (Fig. 2.2).

After confirming the thermal behavior of Mg₂Si, the reaction validity between Mg₂Si and oxide compounds was examined. As mentioned above, this research was inspired by the reaction between Mg₂Si and SiO₂ that belongs to a group IVA oxide; therefore, the reactions between Mg₂Si and other group IVA oxides were first investigated. Group IVA oxides, such as carbon dioxide (CO₂), silicon oxide (SiO₂), germanium oxide (GeO₂), and tin oxide (SnO₂), were employed as the counter

reactants for Mg₂Si. When the reaction feasibility was deduced using the free energy calculation (ΔG) based on the expected reaction formula reaction (2.3), all of the reactions can be considered to be spontaneous at a reaction temperature of 710 °C (Table 2.1).



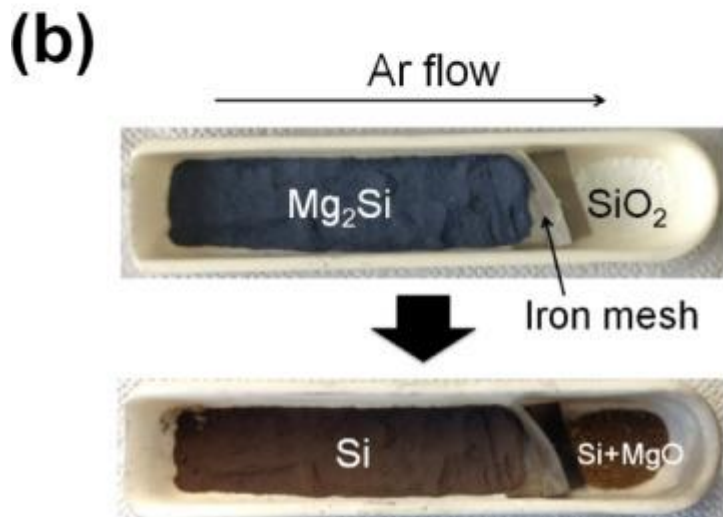
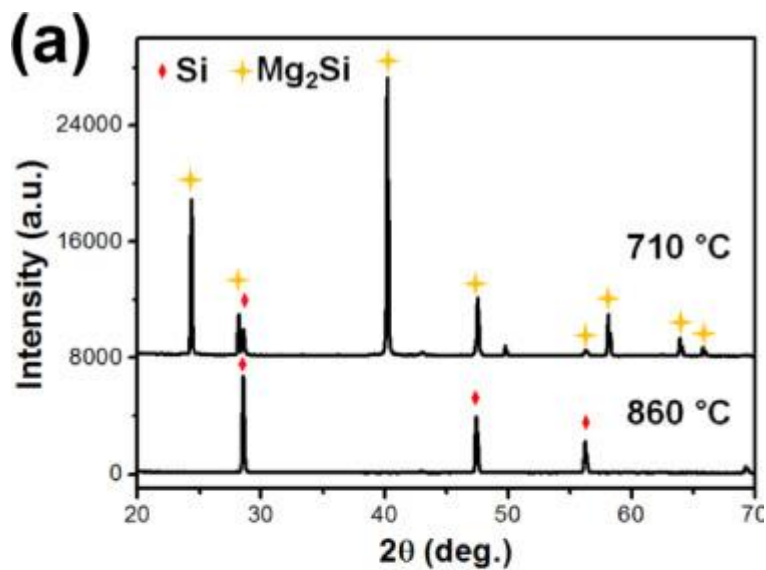


Fig. 2.1 (a) XRD patterns after thermal treatment of pristine commercial Mg₂Si at 710 °C or 860 °C. (b) Photograph before and after treating the pristine Mg₂Si at 860 °C with SiO₂ located beside.

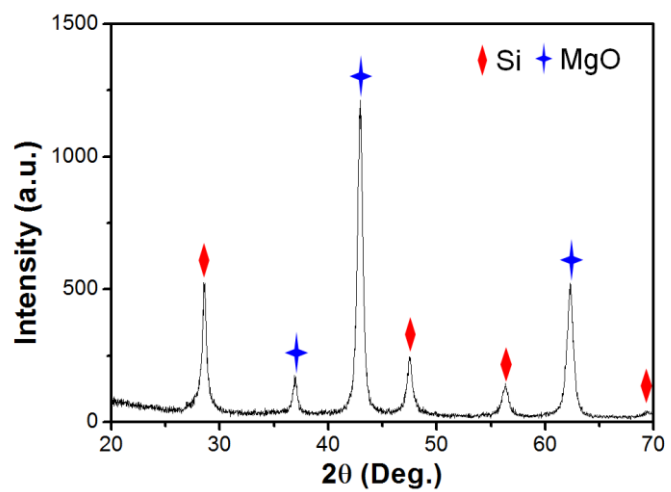


Fig. 2.2 XRD pattern of the crude product obtained from the SiO_2 located next to Mg_2Si after annealing at 860°C .

Table 2.1 Free energy changes of the reactions between Mg₂Si and IVA group oxides.

Reaction	ΔG ^a (kJ)
Mg ₂ Si _(s) + CO _{2(g)} → Si _(s) + C _(s) + 2 MgO _(s)	-518
Mg ₂ Si _(s) + SiO _{2(g)} → 2 Si _(s) + 2 MgO _(s)	-184
Mg ₂ Si _(s) + GeO _{2(g)} → Si _(s) + Ge _(s) + 2 MgO _(s)	-528
Mg ₂ Si _(s) + SnO _{2(g)} → Si _(s) + Sn _(s) + 2 MgO _(s)	-541

^a Calculated at 710 °C

In an attempt to confirm the reaction feasibility, the counter oxides in solid form (SiO_2 , GeO_2 , and SnO_2) were mixed with Mg_2Si and the mixture was annealed at 710 °C for 15 h in a tube furnace under an Ar flow. In the case of CO_2 , CO_2 gas was used instead of Ar. According to XRD analysis (Fig. 2.3c), the results from the reaction of pristine Mg_2Si and SiO_2 clearly showed the patterns of Si and MgO , implying the occurrence of reaction (2.2). When the other solid state reactants (GeO_2 and SnO_2) were employed, the Mg_2Si peaks were hardly observed in the patterns; instead, Si was observed, implying the complete conversion of Mg_2Si . At the same time, magnesium oxide (MgO) and zero-valent metallic species (Ge or Sn) were observed in the XRD patterns (Fig. 2.3d,e), strongly suggesting that the Mg of Mg_2Si reacted with the solid group IVA oxides. On the other hand, when CO_2 was used, Si peak around 29° appeared; however the peak of Mg_2Si was still observed, indicating an incomplete reaction (Fig. 2.3b). This is probably due to the insufficient reaction between solid Mg_2Si and gaseous CO_2 .

It is worth to interpret the resultant crystal phases using a phase diagram. In the case of the reaction between Mg_2Si and GeO_2 , the expected phase from the phase diagrams is a eutectic alloy of Si and Ge (Fig. 2.4a) under the given conditions [2.44]. However, separated phases of Si and Ge are found in the product (Fig. 2.3d). The reason for this phenomenon can be attributed to the slow atomic diffusion kinetics. Namely, the diffusion kinetics of Si into Ge (and *vice versa*) is not sufficient to form a homogeneous mixture of the elements; hence, separated phases are formed. Due to the slow kinetic, only a small degree of alloying which confirms the bonding of Si and Ge at the interface of Si and Ge can be observed in the Raman spectrum (Fig.

2.5). On the other hand, the phase diagram of Si and Sn does not predict an alloy phase of Si and Sn (Fig. 2.4) [2.45]; therefore, separated phases of Si and Sn can thermodynamically form. Moreover, it should be mentioned that Sn melts at the reaction temperature of 710 °C (according to the phase diagram), so the detected Sn crystals would be recrystallized material. Ordinarily, materials formed by magnesiothermic reduction can maintain their original oxide structure via a so-called pseudomorphic transformation [2.26]. However, Sn sequentially goes through melting and recrystallization during the reaction; therefore, the original structure of SnO_2 cannot be preserved. Based on these results, it can be concluded that there is a satisfactory possibility that Si-based composite materials will be produced by adopting Mg_2Si as the reactive Si source and group IVA oxides as the counter reactants.

2.3.2. Design of Reaction System to Synthesize Porous Si@C Composite from Naturally Abundant Sea Sand

It is confirmed that Mg_2Si has potential to be used as a reactive precursor to form Si-based composite materials with Ge or Sn. However, the more generally desired composition for a Si-based anode material is considered to be Si and C. This is because it has been undoubtedly verified that the incorporation of a carbon shell effectively alleviates the pulverization issue by protecting the pulverized particles, improves the electron transferring efficiency to Si, and forms a stable SEI on the carbon surface. Although it was initially expected that the reaction of Mg_2Si and CO_2 would result in Si and C, the reaction between Mg_2Si and CO_2 was confirmed to be

insufficient (Fig. 2.3b). Thus, we attempted to find an alternative way to produce the composite of Si and C from Mg₂Si. Considering the fact that the other group IVA oxides in the solid state completed the reaction (Fig. 2.3c–e), it can be assumed that the solid state reactant enlarges the chance of reaction by providing sufficient time for the reaction to take place. Therefore, we decided to use the solid form of CO₂ (i.e., carbonate). Carbonate is known to be the inorganic solid form of CO₂ in the carbon cycle; hence, it was expected that carbonate would possess analogous reactivity to CO₂. Indeed, calcium carbonate (CaCO₃) and sodium carbonate (Na₂CO₃) have already been proven to be reactive with Mg to form carbon [2.46, 2.47]. Among them, it is known that Na₂CO₃ tends to yield more graphitic carbon [2.47], which shows enhanced electrical conductivity; therefore, Na₂CO₃ was chosen as the alternative reactant. In addition, for the reaction between Mg₂Si and Na₂CO₃, naturally-abundant, sea sand-derived Mg₂Si was adopted. Such a choice of naturally-abundant source is expected to make the process more cost-effective, sustainable, and scalable. Also, as discussed below, a higher void volume fraction can be obtained in the final Si@C composite when compared to that of pristine Mg₂Si, accomplished by removing the MgO that is simultaneously formed during the production of sea sand-derived Mg₂Si.

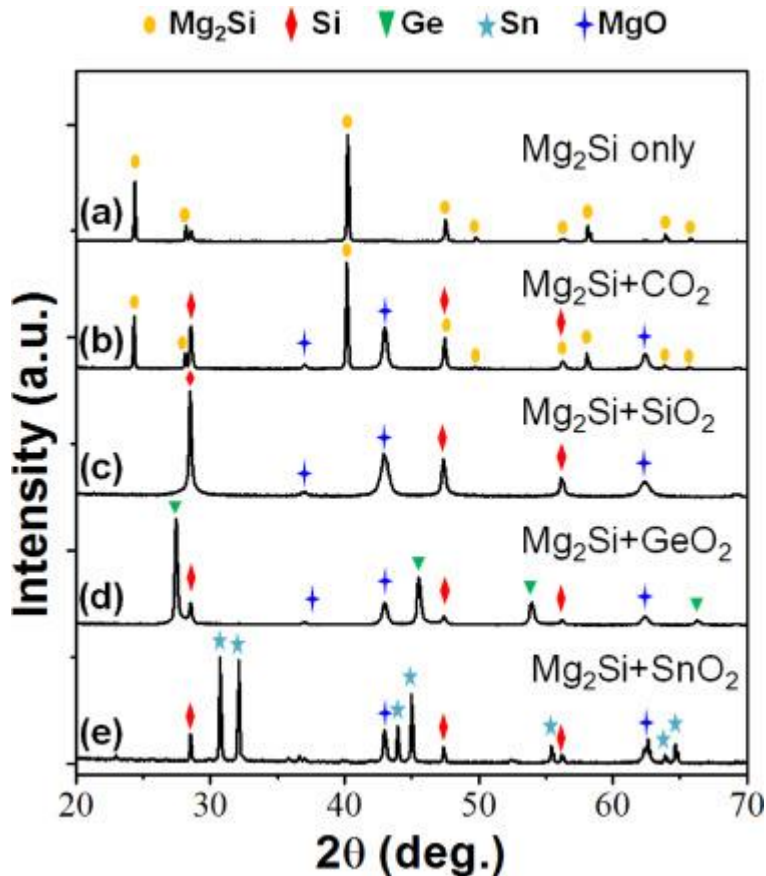


Fig. 2.3 XRD patterns of (a) solely annealed commercial Mg_2Si at $710\text{ }^\circ\text{C}$ for 15 h and the as-reacted products between commercial Mg_2Si and (b) CO_2 , (c) SiO_2 , (d) GeO_2 , and (e) SnO_2 at $710\text{ }^\circ\text{C}$ for 15 h.

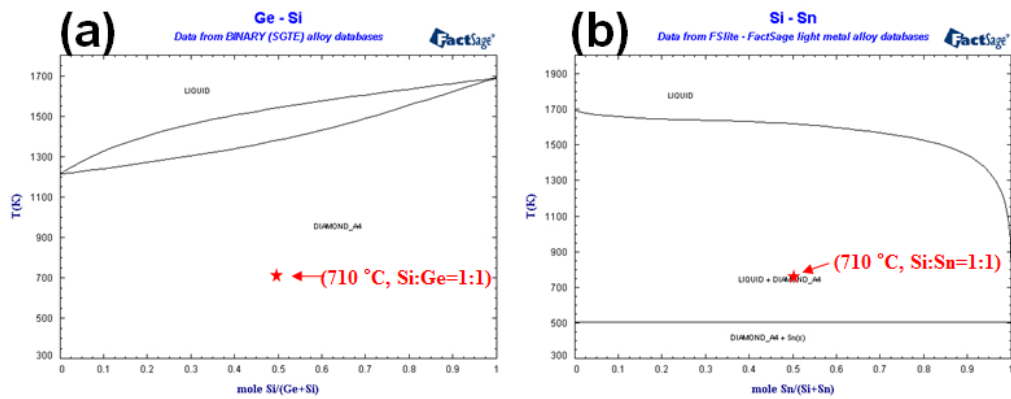


Fig. 2.4 Phase diagrams of (a) Si-Ge [2.44] and (b) Si-Sn [2.45]; a red star is marked at the reaction conditions that were used.

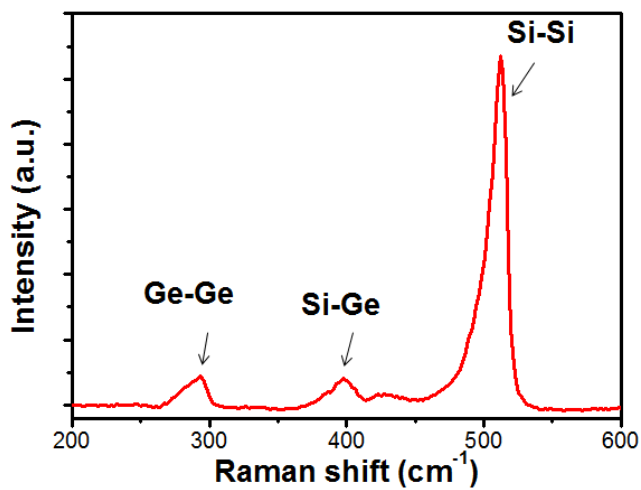
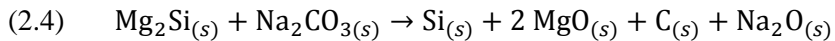


Fig. 2.5 Raman spectrum of the HCl-treated material for the reaction between Mg₂Si and GeO₂ at 710 °C for 15 h.

2.3.3. Understanding of the Reaction between Sea Sand-Derived Mg₂Si and Na₂CO₃

As seen in Fig. 2.6a, the porous Si@C composite material was produced by reacting the sea sand-derived Mg₂Si with Na₂CO₃. Prior to the reaction, sea sand (quartz, Fig. 2.6b) was calcined at 950 °C to remove possible contaminants. The calcined product was ground and sieved with a 500 mesh sieve; this was analyzed by SEM (Fig. 2.7). Then, the sea sand was converted into a composite of Mg₂Si and MgO (sea sand-derived Mg₂Si) by using excess Mg (4.5 equivalents) at 710 °C. XRD analysis showed that the composite of Mg₂Si and MgO was successfully prepared without a quartz peak, implying a high-yield conversion (Fig. 2.6b). Additionally, no aggregation or significant size changes were observed by SEM (Fig. 2.8).

Then, the sea sand-derived Mg₂Si was allowed to react with Na₂CO₃ by simple mixing with grinding and annealing at 710 °C for 5 h. The mole ratio between the reactants (Mg₂Si:Na₂CO₃) was first set to 1:1, according to reaction (2.4), which was based on the previous results that reported the formation of carbon from carbonates.

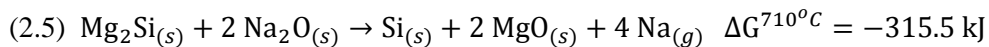


According to XRD analysis of the crude product obtained from the 1:1.0 ratio (Fig. 2.6c), the crystalline phase of Si was identified without the existence of Mg₂Si, implying the conversion of Mg₂Si into Si. However, despite the fact that the ratio of Mg₂Si and Na₂CO₃ was stoichiometric (according to reaction (2.4)), a considerable amount of Na₂CO₃ was still found in the XRD pattern of the 1:1.0 sample (Fig. 2.6c).

Since Mg₂Si has fully disappeared, Na₂CO₃ was excess in reality. Based on this fact, it can be inferred that Mg₂Si can be fully converted with a lower amount of Na₂CO₃. To confirm this hypothesis, the reactions with various reactant ratios (Mg₂Si:Na₂CO₃) from 1:0.8 to 1:0.4 were analyzed by XRD (Fig. 2.6c). It was found that a 1:0.6 ratio of Mg₂Si:Na₂CO₃ can completely convert the Mg₂Si. Therefore, it is concluded that the real stoichiometry is lower than that of the stoichiometry suggested by reaction (2.4).

An unexpected reaction that consumed Mg₂Si in the reaction system was highly speculated. Thus, possible decomposition of the sea sand-derived Mg₂Si was first tested at 710 °C; this was done because pristine Mg₂Si can undergo thermal decomposition at sufficiently high temperatures (Fig. 2.1) or possibly remaining SiO₂ can react with Mg₂Si like reaction (2.2) [2.48]. However, only a small amount of Si was observed in the XRD pattern after this heat treatment (Fig. 2.9), implying that the influence of the self-consumption of Mg₂Si is limited under these conditions.

Another possibility is related to the role of Na₂O; the crystalline phase of Na₂O was not detected in the XRD patterns (Fig. 2.6c). Furthermore, as revealed by ICP experiments, the relative mole amount of Na:Mg was 1.0:0.93 for the initial mixture of commercial mixture of Mg₂Si and Na₂CO₃, and 1.0:0.34 for the annealed mixture, strongly suggesting the decomposition of Na₂O during the reaction. According to previous reports, Na₂O is thermally decomposed to produce O₂ [2.49–2.52], which can oxidize Mg₂Si into Si and MgO according to reaction (2.5).



In order to confirm the role of Na₂O, commercial Mg₂Si and Na₂O (1:2 mole ratio) were mixed by grinding and annealed at 710 °C (Fig. 2.9b). Although a side product of Na₂MgSiO₄ was also formed, the XRD pattern of the product clearly showed that Na₂O can readily oxidize Mg₂Si to produce Si and MgO. As a consequence, it was concluded that the real stoichiometry is lower than that of reaction (2.4); this is due to the unexpected consumption of Mg₂Si by Na₂O and the limited contribution of the self-consumption of Mg₂Si. The real stoichiometry should be in the range of 1:0.5–1:0.6, as deduced from Fig. 2.6c. However, it should also be mentioned that using the real stoichiometry ratio (~1:0.6) for the material preparation is not beneficial for the final application in Li-ion battery anodes. This was the case because the carbon content (12.4 wt%, Fig. 2.10) of the product using a ratio of 1:0.6 was not sufficient to protect the Si anode when used for LIBs (a detailed discussion is available later).

On the other hand, it should be noted that excess amounts of Na₂CO₃ transform Si into Na₂SiO₃ during annealing at 710 °C (Fig. 2.11a). This Na₂SiO₃ can be converted into SiO₂ by an HCl treatment which is needed to remove MgO. Indeed, the appearance of SiO₂ in the IR spectrum was found after the HCl treatment (Fig. 2.11b) [2.53]. Conversion of Si to SiO₂ finally decreases the final Si contents in porous Si@C composite. Therefore, an adequate amount of Na₂CO₃ should be used for the reaction. We adopted a ratio of 1:1 for subsequent experiments.

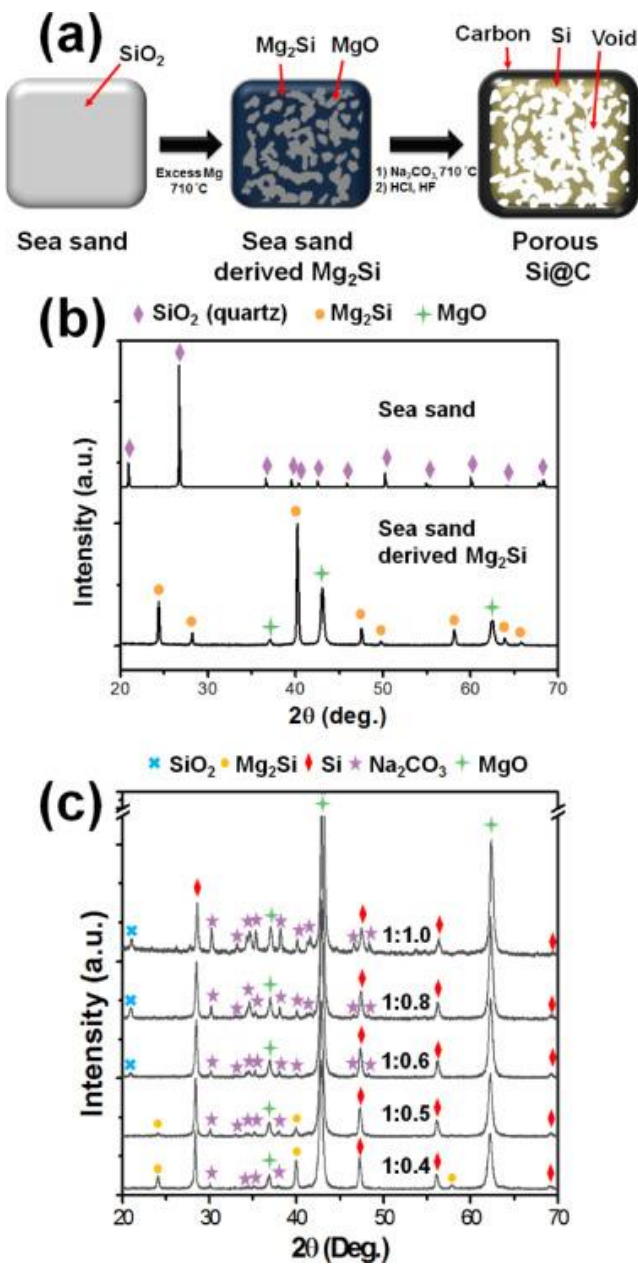


Fig. 2.6 (a) Synthesis scheme from sea sand to porous Si@C via Mg_2Si , (b) XRD patterns of calcined sea sand-derived Mg_2Si , and (c) XRD patterns of the as-reacted material from the reaction between sea sand-derived Mg_2Si and Na_2CO_3 at 710 °C for 5 h with reactant ratios of 1:1.0, 1:0.8, 1:0.6, 1:0.5, and 1:0.4 (Mg₂Si:Na₂CO₃).

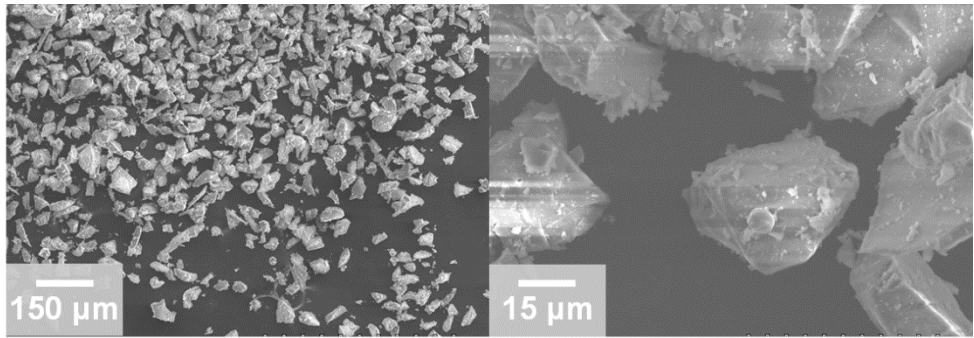


Fig. 2.7 SEM images of sea sand.

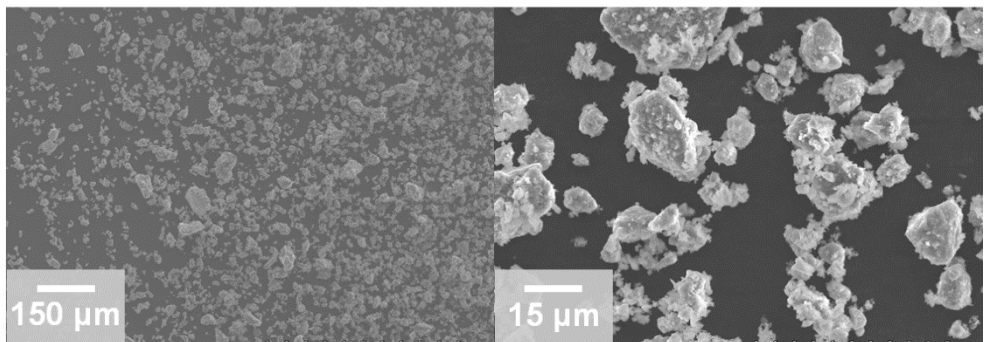


Fig. 2.8 SEM images of sea sand-derived Mg₂Si.

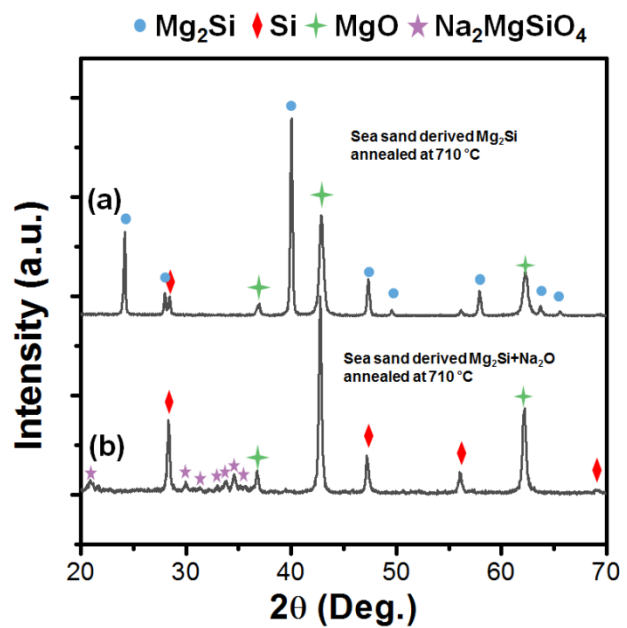


Fig. 2.9 XRD patterns of (a) sea sand-derived Mg_2Si annealed at 710°C for 15 h and (b) mixture of commercial Mg_2Si and Na_2O with a molar ratio of 1:2.0 annealed at 710°C for 5 h.

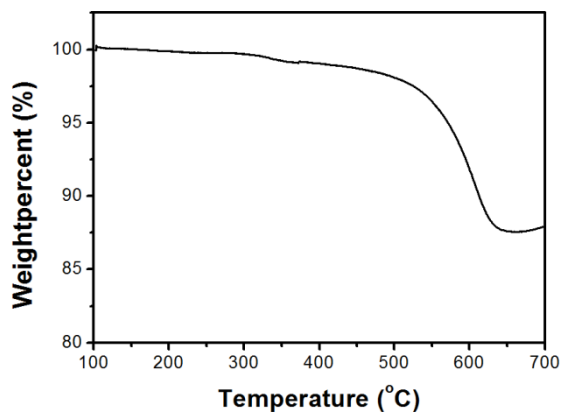


Fig. 2.10 TGA plot of porous Si@C-0.6 produced with a sea sand-derived Mg₂Si:Na₂CO₃ ratio of 1:0.6.

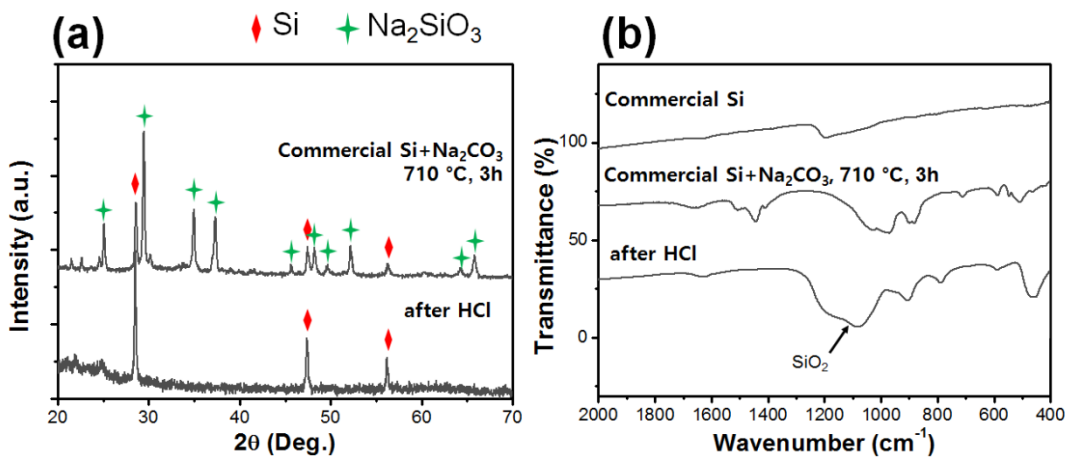


Fig. 2.11 (a) XRD patterns of as-reacted and HCl-treated products from the reaction between commercial Si and Na₂CO₃ (1:1 mole ratio) at 710 °C for 3 h and (b) IR spectra of commercial Si, as-reacted product, and HCl-treated products from the reaction between commercial Si and Na₂CO₃ at 710 °C for 3 h.

2.3.4. Confirmation of Composition and Morphology of Porous Si@C

After reaction of the sea sand-derived Mg₂Si and Na₂CO₃ (1:1 mole ratio, porous Si@C-1) and subsequent treatments with HCl and HF, a single pattern of Si in the porous Si@C-1 was shown in the XRD results (Fig. 2.12a). According to the TGA analysis for the acid-treated sample (Fig. 2.12b), the typical combustion pattern of carbon (with 25.2 wt% carbon) was observed; elemental analysis confirmed a carbon content of 30.2 wt%. The difference in these carbon contents is believed to have originated from the oxidation of Si during TGA analysis, which causes weight gain in the sample. Thus, the carbon content can be underestimated in TGA. Compared to the porous Si@C obtained from a 1:0.6 ratio (porous Si@C-0.6, Fig. 2.10), the higher amount of Na₂CO₃ results in a higher carbon content. Raman spectroscopy measurements were also performed (Fig. 2.12c). Peaks attributed to Si and carbon (D and G bands) were found in the Raman spectrum, confirming the formation of the composite of Si and C [2.29].

The morphological features of acid-treated Si@C-1 were monitored by SEM and TEM measurements (Fig. 2.12d,e). A several-micrometer-sized pouch, containing both solid material and void space, was clearly identified. This can be assigned to the formation of carbon-coated porous Si nanostructures (Fig. 2.12d,e and Fig. 2.13). Furthermore, the TEM-EDX mapping data for porous Si@C-1 undoubtedly showed that the interior solid material is Si and the shell of the pouch is carbon (Fig. 2.12f,g). In addition, the d-spacing of the lattice for the interior solid material was 3.1 Å, corresponding to the (111) plane of Si (Fig. 2.12h). Selected area electron

diffraction (SAED) was used to reveal the crystalline features of the interior Si (Fig. 2.12i). It is noted that the obtained structure clearly matches the desired structure of a Si-based anode material (as described previously).

Its formation mechanism can be explained as follows. First, the reaction between Mg_2Si and Na_2CO_3 only occurs at the surface of Mg_2Si , resulting in Si encapsulated within carbon. At the given reaction temperature, the Mg in Mg_2Si possesses reducibility and mobility [2.41, 2.43, 2.52, 2.54, 2.55], but it does not easily escape from Mg_2Si through thermal decomposition (Fig. 2.1 and Fig. 2.9a). Thus, the only place where Mg in Mg_2Si can encounter Na_2CO_3 is the surface of Mg_2Si where physical contact between Mg_2Si and Na_2CO_3 is attained. At the early stage of the reaction, Mg in the outer region of Mg_2Si , in contact with Na_2CO_3 , should be firstly consumed by the reaction (2.4). At the meantime, due to the consumption, there should be a gradation of Mg concentration through Mg_2Si , higher at the core and lower at the shell. Accordingly, net diffusion flux of Mg should be directed from the core to the surface of Mg_2Si . By this phenomenon, Mg can be constantly supplied for the reaction (2.4) that occurs at the surface of Mg_2Si , resulting in the formation of a carbon layer along the Mg_2Si surface. Also, such a consumption of Mg by surface reaction and outward diffusion turns Mg_2Si into Si. Therefore, the Si transformed from the sea sand-derived Mg_2Si can be located inside of a carbon shell.

Additionally, the void space in the carbon can be attributed to two factors. First, the MgO contained in the sea sand-derived Mg_2Si was leached out during the acid

treatment; hence, this turns into void space. In addition, TEM images for the as-reacted sample of Si@C before acid-treatment already presents void space inside of the carbon (Fig. 2.14), implying there is a void forming mechanism discriminated from MgO etching. Probably, the diffusion of labile Mg in Mg₂Si to the outside while reducing carbonate to carbon at the surface of Mg₂Si generates void space inside the carbon shell. Other reports have shown that macroporous Si or Ge can be produced by eliminating the metal source in Mg₂Si and Ca_xGe [2.56, 2.57].

It is worth to mention that utilizing sea sand-derived Mg₂Si is advantageous to the commercial Mg₂Si in terms of void formation. When pristine commercial Mg₂Si is converted into Si, it forms a void space that is only derived from the space that was occupied by Mg of Mg₂Si. The volume of the void space can be calculated to be 221% of the volume of Si (see Supporting Information for calculation details). In contrast, sea sand (quartz) can be transformed into Mg₂Si and MgO via reaction with excess Mg, as seen in reaction (2.1) [2.58]. MgO embedded in Mg₂Si can also turn into void space, as mentioned above, after the acid treatment in the final process. Our calculations suggest that the possible void space that can be generated in the final product from the SiO₂-derived Mg₂Si is 409% of the volume of Si; this value seems appropriate to accommodate the Si volume change in applications.

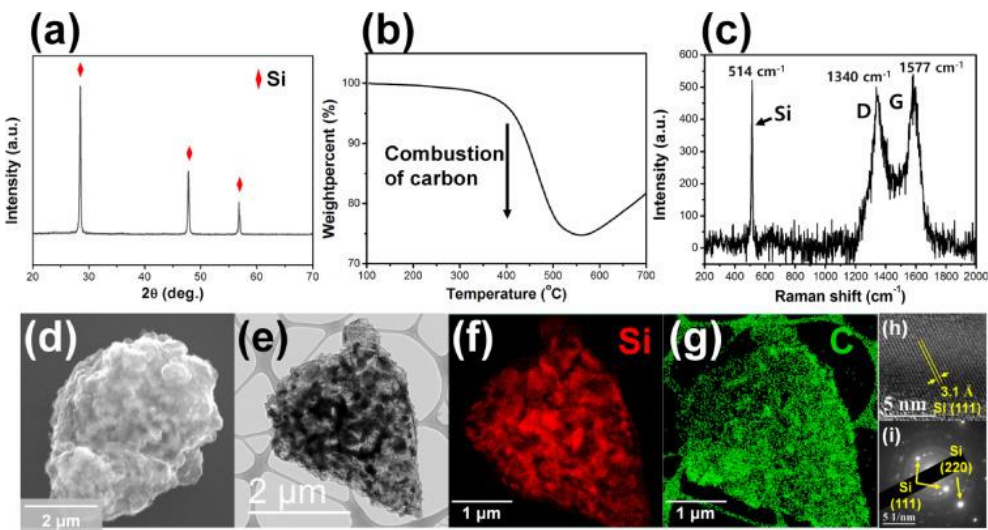


Fig. 2.12 (a) XRD pattern, (b) TGA plot, (c) Raman spectrum, (d) SEM image, (e) TEM image, (f) TEM-EDX Si map, (g) TEM-EDX C map, (h) HR-TEM image, and (i) SAED pattern of HCl- and HF-treated materials from the reaction between the sea sand-derived Mg₂Si and Na₂CO₃ with a ratio of 1:1 at 710 °C 5 h (porous Si@C-1).

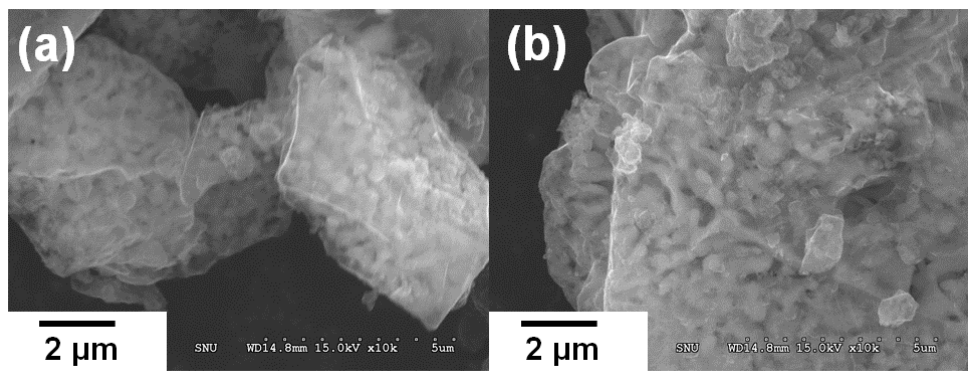


Fig. 2.13 SEM image of acid-treated products from the reaction between commercial Si and Na₂CO₃ (1:1 mole ratio) at 710 °C for 5 h; it can be clearly seen that porous Si is encapsulated in a carbon shell.

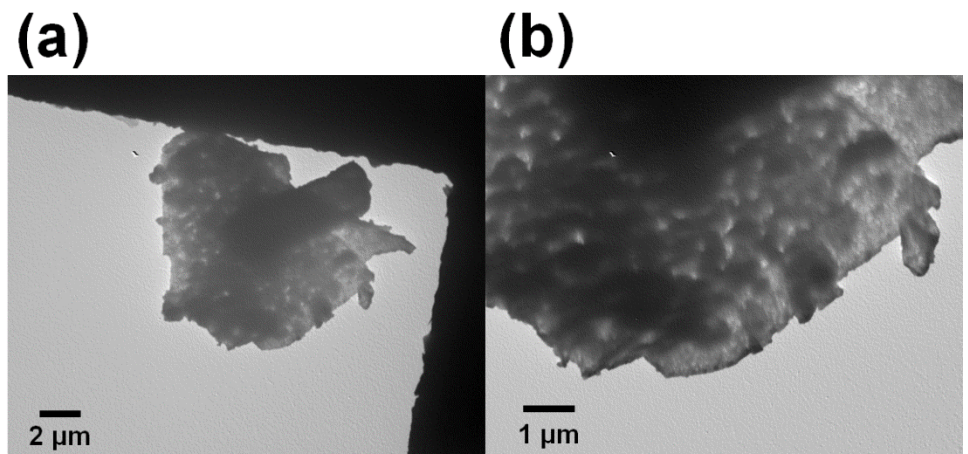


Fig. 2.14 (a, b) TEM images of as-reacted material from the sea sand-derived Mg_2Si and Na_2CO_3 .

2.3.5. Electrochemical Characterization of Porous Si@C

The porous Si@C was then employed as anodes for LIBs. Half-cell testing was conducted by adopting Li metal as the counter electrode within a voltage range of 0.01-1.2 V, and the cycling performance at a rate of 0.4 A/g was measured. Both porous Si@C samples (porous Si@C-0.6 and 1, produced from 1:0.6 and 1:1 ratios of sea sand-derived Mg₂Si and Na₂CO₃, respectively) were investigated and compared (Fig. 2.15a). It was clearly observed that porous Si@C-0.6 is more unstable in terms of its cycling stability compared to porous Si@C-1. Porous Si@C-0.6 presented an initial reversible capacity 2615 mAh/g, which is much larger than that of porous Si@C-1. However, the capacity of porous Si@C-0.6 was radically decreased and eventually showed a lower reversible capacity than porous Si@C-1 after a few cycles. Furthermore, in the case of porous Si@C-1, the reversible capacity stayed near 1000 mAh/g, even after 200 cycles, with a rate of 0.4 A/g. When comparing the voltage profiles after several cycles for both materials, the observed differences in the cycling stability can be attributed to the differences in the ability to prevent pulverization of Si. In the charging (delithiation) profiles of both materials, two distinguishable plateaus at ~0.3 V and ~0.4 V were observed (Fig. 2.15b,c). The relative length of the two plateaus is related to the particle size of Si [2.59]. The plateau at ~0.3 V can be lengthened when the particle size of Si is reduced, whereas the plateau at ~0.4 V is lengthened when the Si particle size is increased. Due to this, the absence of the lower plateau in the initial delithiation curves indicates larger Si particles. As cycling proceeds, Si particles are pulverized into smaller particles; therefore, the lower plateau is lengthened. This tendency is observed for both porous

Si@C materials. However, it can be noted that the shortening in the upper plateau is sufficiently compensated for by the lengthening of the lower plateau in porous Si@C-1; while porous Si@C-0.6 cannot compensate for this shortening. In other words, the pulverized Si particles in Si@C-1 can still participate in the reversible reaction, while those in Si@C-0.6 are disconnected from the current pathway. The origin of this phenomenon can be attributed to the difference in the carbon amount, as mentioned above (Fig. 2.10 and Fig. 2.12). Furthermore, the rate capability of porous Si@C-1 was investigated by varying the charge-discharge rate from 0.4 A/g to 10 A/g (Fig. 2.16). Remarkably, porous Si@C showed a reversible capacity of nearly 700 mAh/g at a high rate of 4 A/g. Also, there was no catastrophic breakdown of the cell, even when a rate as high as 10 A/g was used. Overall, it can be concluded that porous Si@C show potential as anode materials for Li-ion batteries. Because of the great advantages of the synthetic procedures of these materials, they should be further investigated for the realization of high-functioning materials.

Additionally, it is worth noting that another composite material, porous Si@Ge, that can be synthesized by our approach was also successfully applied to the electrochemical test. For the synthesis, briefly, pristine Mg₂Si was wrapped by GeO₂ matrix and annealed at 710 °C (Fig. 2.17a, See Experimental section for details). After HCl treatment, metallic Si and Ge were clearly confirmed by XRD (Fig. 2.17b). The SEM images of the material visualized the intriguing structure of porous Si encapsulated by Ge (Fig. 2.17c-e). When half-cell test was conducted within a voltage range of 0.01-1.2 V. It was found that porous Si@Ge shows a capacity of nearly 1800 mAh/g at the initial cycle and maintains a reversible capacity

of ~1050 mAh/g at the 70th at a rate of 0.4 A/g (Fig. 2.17f). Also, the rate capability of porous Si@Ge was examined at current densities between 0.4 A/g and 4.0 A/g. Porous Si@Ge showed a reversible capacity of ~510 mAh/g, even at the 4.0 A/g (Fig. 2.17g). This demonstration confirms the versatility of our approach.

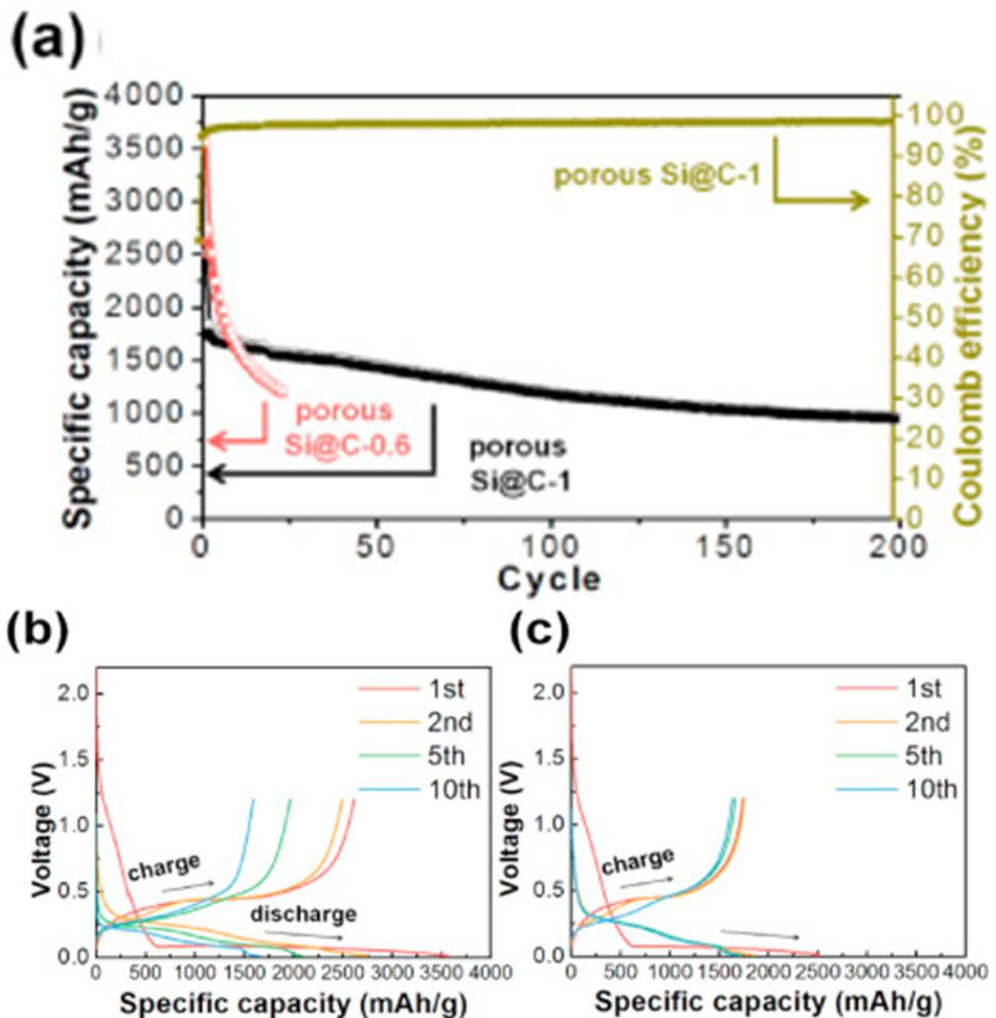


Fig. 2.15 (a) Cycling performance of porous Si@C-0.6 and porous Si@C-1 synthesized with Mg₂Si:Na₂CO₃ ratios of 1:0.6 and 1:1. Voltage profiles of (b) porous Si@C-0.6 and (c) porous Si@C-1 extracted from the cycling performance test at 0.4 A/g. (Note that all of the capacity values are calculated based on the mass of the porous Si@C composites.).

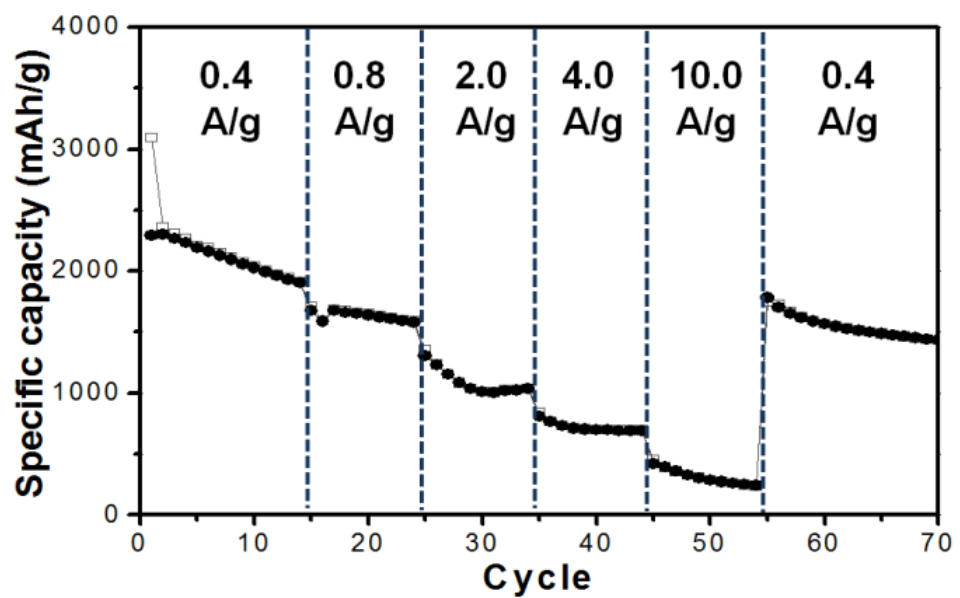


Fig. 2.16 Rate capability of porous Si@C-1.

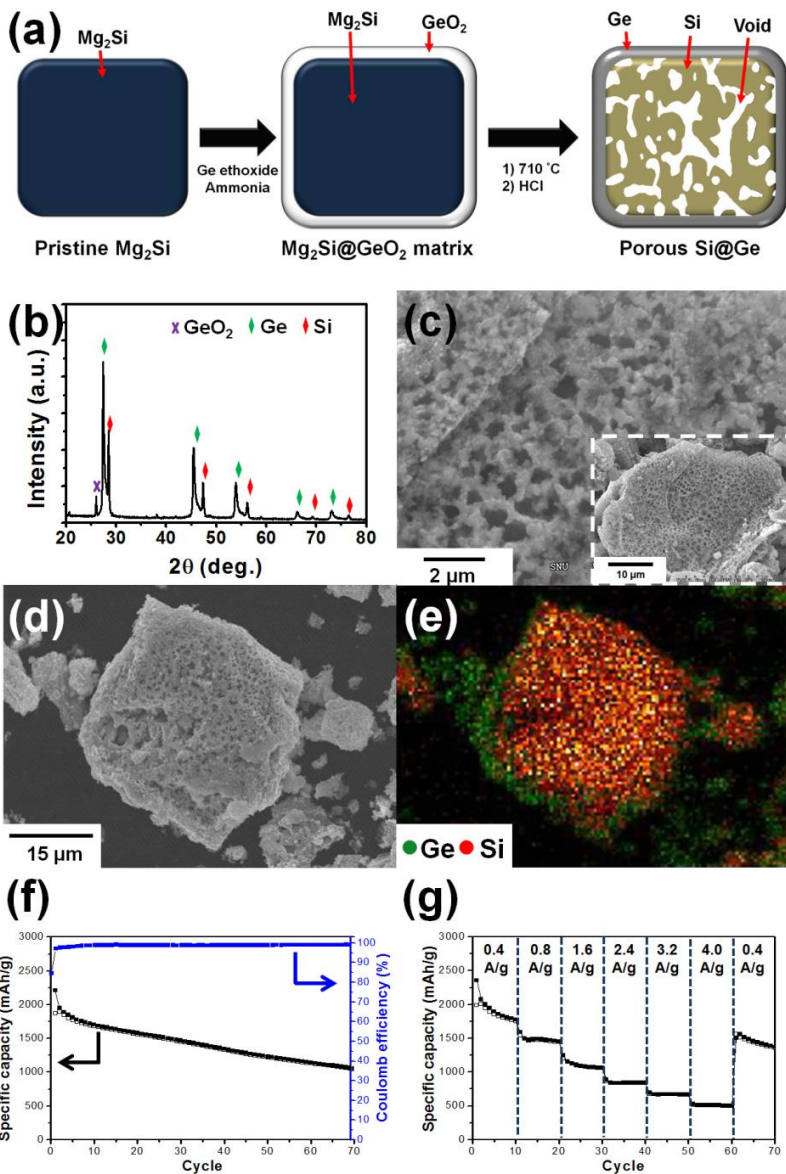


Fig. 2.17 (a) Schematic of the preparation of porous Si@Ge that employs Mg_2Si as a reactive Si source and GeO_2 , (b) XRD pattern, (c) SEM image of central region (inset: low-magnification image), and (d-e) SEM-EDX mapping data of porous Si@Ge, (f) cycling performance of porous Si@Ge at a current density of 0.4 A/g, and (g) rate performance of porous Si@Ge.

2.4. Conclusion

The utilization of Mg₂Si as a reactive source for Si-based composite materials was investigated. The lability and reducibility of Mg₂Si enabled it to reduce various kinds of oxide materials and carbonate (e.g., SiO₂, GeO₂, SnO₂, and Na₂CO₃). As a result, a composite of Si (produced from Mg₂Si) and the reduced products of the counter reactant (including Ge, Sn, and C) were obtained. Our results imply that the reaction of Mg₂Si is versatile; thus, other kinds of counter reactant oxides, such as transition metal oxides, could also be adopted.

Using the chemistry of Mg₂Si, porous Si was wrapped by C to form a composite that is attractive for the anode material of LIBs. The reaction procedure is based on simple solid state reactions using readily-available reactants. Also, as demonstrated in the case of porous Si@C, naturally-abundant substances, such as sea sand, can be used as the initial Si source, augmenting cost-effectiveness, sustainability, and scalability to this process. Despite the simplicity of the preparation procedure, reasonable electrochemical performances were obtained from the prepared composite materials. Thus, it is expected that our procedure can be utilized for the mass-scale production of Si-based composite materials.

2.5. References

- [2.1] Wu, H. and Y. Cui, "Designing nanostructured Si anodes for high energy lithium ion batteries", *Nano Today*, **2012**, 7, 414.
- [2.2] Liu, X. H., L. Zhong, S. Huang, S. X. Mao, T. Zhu and J. Y. Huang, "Size-dependent fracture of silicon nanoparticles during lithiation", *ACS Nano*, **2012**, 6, 1522.
- [2.3] Park, C. M., J. H. Kim, H. Kim and H. J. Sohn, "Li-alloy based anode materials for Li secondary batteries", *Chemical Society Reviews*, **2010**, 39, 3115.
- [2.4] Wu, H., G. Chan, J. W. Choi, I. Ryu, Y. Yao, M. T. McDowell, S. W. Lee, A. Jackson, Y. Yang, L. Hu and Y. Cui, "Stable cycling of double-walled silicon nanotube battery anodes through solid-electrolyte interphase control", *Nature Nanotechnology*, **2012**, 7, 310.
- [2.5] Wu, H., G. Zheng, N. Liu, T. J. Carney, Y. Yang and Y. Cui, "Engineering empty space between Si nanoparticles for lithium-ion battery anodes", *Nano Letters*, **2012**, 12, 904.
- [2.6] Chan, C. K., H. Peng, G. Liu, K. McIlwrath, X. F. Zhang, R. A. Huggins and Y. Cui, "High-performance lithium battery anodes using silicon nanowires", *Nature Nanotechnology*, **2008**, 3, 31.
- [2.7] Yao, Y., M. T. McDowell, I. Ryu, H. Wu, N. Liu, L. Hu, W. D. Nix and Y. Cui,

"Interconnected silicon hollow nanospheres for lithium-ion battery anodes with long cycle life", *Nano Letters*, **2011**, *11*, 2949.

[2.8] Kim, H., B. Han, J. Choo and J. Cho, "Three-dimensional porous silicon particles for use in high-performance lithium secondary batteries", *Angewandte Chemie - International Edition*, **2008**, *47*, 10151.

[2.9] Wang, B., X. Li, X. Zhang, B. Luo, Y. Zhang and L. Zhi, "Contact-engineered and void-involved silicon/carbon nanohybrids as lithium-ion-battery anodes", *Advanced Materials*, **2013**, *25*, 3560.

[2.10] Liu, N., H. Wu, M. T. McDowell, Y. Yao, C. Wang and Y. Cui, "A yolk-shell design for stabilized and scalable Li-ion battery alloy anodes", *Nano Letters*, **2012**, *12*, 3315.

[2.11] Liu, N., Z. Lu, J. Zhao, M. T. McDowell, H. W. Lee, W. Zhao and Y. Cui, "A pomegranate-inspired nanoscale design for large-volume-change lithium battery anodes", *Nature Nanotechnology*, **2014**, *9*, 187.

[2.12] Pan, L., H. Wang, D. Gao, S. Chen, L. Tan and L. Li, "Facile synthesis of yolk-shell structured Si-C nanocomposites as anodes for lithium-ion batteries", *Chemical Communications*, **2014**, *50*, 5878.

[2.13] Hu, Y. S., R. Demir-Cakan, M. M. Titirici, J. O. Müller, R. Schlögl, M. Antonietti and J. Maier, "Superior storage performance of a Si@SiO_x/C nanocomposite as anode material for lithium-ion batteries", *Angewandte Chemie -*

International Edition, **2008**, *47*, 1645.

[2.14] Zhang, Z., Y. Wang, W. Ren, Q. Tan, Y. Chen, H. Li, Z. Zhong and F. Su, "Scalable synthesis of interconnected porous silicon/carbon composites by the rochow reaction as high-performance anodes of lithium ion batteries", *Angewandte Chemie - International Edition*, **2014**, *53*, 5165.

[2.15] Hwang, T. H., Y. M. Lee, B. S. Kong, J. S. Seo and J. W. Choi, "Electrospun core-shell fibers for robust silicon nanoparticle-based lithium ion battery anodes", *Nano Letters*, **2012**, *12*, 802.

[2.16] Ahn, J., K. J. Lee, W. Bak, J. J. Kim, J. K. Lee, W. C. Yoo and Y. E. Sung, "Elucidating relationships between structural properties of nanoporous carbonaceous shells and electrochemical performances of si@carbon anodes for lithium-ion batteries", *Journal of Physical Chemistry C*, **2015**, *119*, 10255.

[2.17] Yu, Y., L. Gu, C. Zhu, S. Tsukimoto, P. A. Van Aken and J. Maier, "Reversible storage of lithium in silver-coated three-dimensional macroporous silicon", *Advanced Materials*, **2010**, *22*, 2247.

[2.18] Chen, D., X. Mei, G. Ji, M. Lu, J. Xie, J. Lu and J. Y. Lee, "Reversible lithium-ion storage in silver-treated nanoscale hollow porous silicon particles", *Angewandte Chemie - International Edition*, **2012**, *51*, 2409.

[2.19] Park, Y., N. S. Choi, S. Park, S. H. Woo, S. Sim, B. Y. Jang, S. M. Oh, S. Park, J. Cho and K. T. Lee, "Si-encapsulating hollow carbon electrodes via

electroless etching for lithium-ion batteries", *Advanced Energy Materials*, **2013**, *3*, 206.

[2.20] Song, T., H. Cheng, H. Choi, J. H. Lee, H. Han, D. H. Lee, D. S. Yoo, M. S. Kwon, J. M. Choi, S. G. Doo, H. Chang, J. Xiao, Y. Huang, W. I. Park, Y. C. Chung, H. Kim, J. A. Rogers and U. Paik, "Si/Ge double-layered nanotube array as a lithium ion battery anode", *ACS Nano*, **2012**, *6*, 303.

[2.21] Kim, Y. M., J. Ahn, S. H. Yu, D. Y. Chung, K. J. Lee, J. K. Lee and Y. E. Sung, "Titanium silicide coated porous silicon nanospheres as anode materials for lithium ion batteries", *Electrochimica Acta*, **2015**, *151*, 256.

[2.22] Wang, W. and P. N. Kumta, "Nanostructured hybrid silicon/carbon nanotube heterostructures: Reversible high-capacity lithium-ion anodes", *ACS Nano*, **2010**, *4*, 2233.

[2.23] Magasinski, A., P. Dixon, B. Hertzberg, A. Kvitt, J. Ayala and G. Yushin, "High-performance lithium-ion anodes using a hierarchical bottom-up approach", *Nature Materials*, **2010**, *9*, 353.

[2.24] Bang, B. M., H. Kim, H. K. Song, J. Cho and S. Park, "Scalable approach to multi-dimensional bulk Si anodes via metal-assisted chemical etching", *Energy and Environmental Science*, **2011**, *4*, 5013.

[2.25] Vlad, A., A. L. M. Reddy, A. Ajayan, N. Singh, J. F. Gohy, S. Melinte and P. M. Ajayan, "Roll up nanowire battery from silicon chips", *Proceedings of the*

National Academy of Sciences of the United States of America, **2012**, *109*, 15168.

- [2.26] Bao, Z., M. R. Weatherspoon, S. Shian, Y. Cai, P. D. Graham, S. M. Allan, G. Ahmad, M. B. Dickerson, B. C. Church, Z. Kang, H. W. Abernathy Iii, C. J. Summers, M. Liu and K. H. Sandhage, "Chemical reduction of three-dimensional silica micro-assemblies into microporous silicon replicas", *Nature*, **2007**, *446*, 172.
- [2.27] Zhang, R., Y. Du, D. Li, D. Shen, J. Yang, Z. Guo, H. K. Liu, A. A. Elzatahry and D. Zhao, "Highly reversible and large lithium storage in mesoporous Si/C nanocomposite anodes with silicon nanoparticles embedded in a carbon framework", *Advanced Materials*, **2014**, *26*, 6749.
- [2.28] Ru, Y., D. G. Evans, H. Zhu and W. Yang, "Facile fabrication of yolk-shell structured porous Si-C microspheres as effective anode materials for Li-ion batteries", *RSC Advances*, **2014**, *4*, 71.
- [2.29] Li, W., Y. Tang, W. Kang, Z. Zhang, X. Yang, Y. Zhu, W. Zhang and C. S. Lee, "Core-Shell Si/C Nanospheres Embedded in Bubble Sheet-like Carbon Film with Enhanced Performance as Lithium Ion Battery Anodes", *Small*, **2015**, *11*, 1345.
- [2.30] Li, W., Z. Li, W. Kang, Y. Tang, Z. Zhang, X. Yang, H. Xue and C. S. Lee, "Hollow nanospheres of loosely packed Si/SiO_x nanoparticles encapsulated in carbon shells with enhanced performance as lithium ion battery anodes", *Journal of Materials Chemistry A*, **2014**, *2*, 12289.
- [2.31] Liu, N., K. Huo, M. T. McDowell, J. Zhao and Y. Cui, "Rice husks as a

sustainable source of nanostructured silicon for high performance Li-ion battery anodes", *Scientific Reports*, **2013**, *3*, 1919.

[2.32] Jung, D. S., M. H. Ryou, Y. J. Sung, S. B. Park and J. W. Choi, "Recycling rice husks for high-capacity lithium battery anodes", *Proceedings of the National Academy of Sciences of the United States of America*, **2013**, *110*, 12229.

[2.33] Yoo, J. K., J. Kim, M. J. Choi, Y. U. Park, J. Hong, K. M. Baek, K. Kang and Y. S. Jung, "Extremely high yield conversion from low-cost sand to high-capacity Si electrodes for Li-ion batteries", *Advanced Energy Materials*, **2014**, *4*, 1400622.

[2.34] Favors, Z., W. Wang, H. H. Bay, Z. Muthu, K. Ahmed, C. Liu, M. Ozkan and C. S. Ozkan, "Scalable synthesis of nano-silicon from beach sand for long cycle life Li-ion batteries", *Scientific Reports*, **2014**, *4*, 5623.

[2.35] Liu, J., P. Kopold, P. A. vanAken, J. Maier and Y. Yu, "Energy Storage Materials from Nature through Nanotechnology: A Sustainable Route from Reed Plants to a Silicon Anode for Lithium-Ion Batteries", *Angewandte Chemie - International Edition*, **2015**, *54*, 9632.

[2.36] Ryu, J., D. Hong, S. Choi and S. Park, "Synthesis of Ultrathin Si Nanosheets from Natural Clays for Lithium-Ion Battery Anodes", *ACS Nano*, **2016**, *10*, 2843.

[2.37] Kim, W. S., Y. Hwa, J. H. Shin, M. Yang, H. J. Sohn and S. H. Hong, "Scalable synthesis of silicon nanosheets from sand as an anode for Li-ion batteries", *Nanoscale*, **2014**, *6*, 4297.

[2.38] Van Buuren, M. R. J., F. Voermans and H. Van Kempen, "Bonding in Mg₂Si studied with X-ray photoelectron spectroscopy", *Journal of Physical Chemistry*, **1995**, *99*, 9519.

[2.39] Ahn, J., H. S. Kim, J. Pyo, J. K. Lee and W. C. Yoo, "Variation in Crystalline Phases: Controlling the Selectivity between Silicon and Silicon Carbide via Magnesiothermic Reduction using Silica/Carbon Composites", *Chemistry of Materials*, **2016**, *28*, 1526.

[2.40] Nguyen, T. D., J. A. Kelly, W. Y. Hamad and M. J. MacLachlan, "Magnesiothermic reduction of thin films: Towards semiconducting chiral nematic mesoporous silicon carbide and silicon structures", *Advanced Functional Materials*, **2015**, *25*, 2175.

[2.41] Lin, N., L. Wang, J. Zhou, J. Zhou, Y. Han, Y. Zhu, Y. Qian and C. Cao, "A Si/Ge nanocomposite prepared by a one-step solid-state metathesis reaction and its enhanced electrochemical performance", *Journal of Materials Chemistry A*, **2015**, *3*, 11199.

[2.42] Lin, N., J. Zhou, Y. Han, K. Zhang, Y. Zhu and Y. Qian, "Chemical synthesis of porous hierarchical Ge-Sn binary composites using metathesis reaction for rechargeable Li-ion batteries", *Chemical Communications*, **2015**, *51*, 17156.

[2.43] Chu, W. K., S. S. Lau, J. W. Mayer, H. Müller and K. N. Tu, "Implanted noble gas atoms as diffusion markers in silicide formation", *Thin Solid Films*, **1975**, *25*,

393.

[2.44] Olesinski, R. W. and G. J. Abbaschian, "The Ge-Si (Germanium-Silicon) system", *Bulletin of Alloy Phase Diagrams*, **1984**, 5, 180.

[2.45] Feutelais, Y., B. Legendre and S. G. Fries, "Thermodynamic evaluation of the system Germanium - Tin", *Calphad: Computer Coupling of Phase Diagrams and Thermochemistry*, **1996**, 20, 109.

[2.46] Zhao, J., Y. Guo, Z. Li, Q. Guo, J. Shi, L. Wang and J. Fan, "An approach for synthesizing graphene with calcium carbonate and magnesium", *Carbon*, **2012**, 50, 4939.

[2.47] Wang, J., R. Ma, Z. Zhou, G. Liu and Q. Liu, "Magnesiothermic synthesis of sulfur-doped graphene as an efficient metal-free electrocatalyst for oxygen reduction", *Scientific Reports*, **2015**, 5, 9304.

[2.48] Yamada, T., H. Itahara and H. Yamane, "Preparation of micro-porous Si particles from Mg₂Si powder", *Materials Letters*, **2013**, 98, 157.

[2.49] Kim, J. W. and H. G. Lee, "Thermal and carbothermic decomposition of Na₂CO₃ and Li₂CO₃", *Metallurgical and Materials Transactions B: Process Metallurgy and Materials Processing Science*, **2001**, 32, 17.

[2.50] Motzfeldt, K., "The thermal decomposition of sodium carbonate by the effusion method", *Journal of Physical Chemistry*, **1955**, 59, 139.

- [2.51] Liang, J., X. Li, Z. Hou, W. Zhang, Y. Zhu and Y. Qian, "A Deep Reduction and Partial Oxidation Strategy for Fabrication of Mesoporous Si Anode for Lithium Ion Batteries", *ACS Nano*, **2016**, *10*, 2295.
- [2.52] Liang, J., X. Li, Z. Hou, C. Guo, Y. Zhu and Y. Qian, "Nanoporous silicon prepared through air-oxidation demagnesiation of Mg₂Si and properties of its lithium ion batteries", *Chemical Communications*, **2015**, *51*, 7230.
- [2.53] Yoo, B. U., M. H. Han, H. H. Nersisyan, J. H. Yoon, K. J. Lee and J. H. Lee, "Self-templated synthesis of hollow silica microspheres using Na₂SiO₃ precursor", *Microporous and Mesoporous Materials*, **2014**, *190*, 139.
- [2.54] Hou, Z., X. Zhang, J. Liang, X. Lia, X. Yan, Y. Zhu and Y. Qian, "Synchronously synthesized Si@C composites through solvothermal oxidation of Mg₂Si as lithium ion battery anode", *RSC Advances*, **2015**, *5*, 71355.
- [2.55] Wang, L., N. Lin, J. Zhou, Y. Zhu and Y. Qian, "Silicon nanoparticles obtained via a low temperature chemical "metathesis" synthesis route and their lithium-ion battery properties", *Chemical Communications*, **2015**, *51*, 2345.
- [2.56] Xiao, C., N. Du, X. Shi, H. Zhang and D. Yang, "Large-scale synthesis of Si@C three-dimensional porous structures as high-performance anode materials for lithium-ion batteries", *Journal of Materials Chemistry A*, **2014**, *2*, 20494.
- [2.57] Yin, H., W. Xiao, X. Mao, H. Zhu and D. Wang, "Preparation of a porous nanostructured germanium from GeO₂ via a "reduction-alloying-dealloying"

approach", *Journal of Materials Chemistry A*, **2015**, *3*, 1427.

[2.58] Li, W., Q. Yang and H. Tatsuoka, "Synthesis of Mg₂Si/MgO nanofibers using SiO₂ nanofibers in Mg vapor", *e-Journal of Surface Science and Nanotechnology*, **2012**, *10*, 297.

[2.59] Gauthier, M., J. Danet, B. Lestriez, L. Roué, D. Guyomard and P. Moreau, "Nanoscale compositional changes during first delithiation of Si negative electrodes", *Journal of Power Sources*, **2013**, 227, 237.

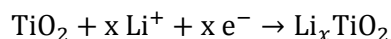
3. Engineering titanium dioxide nanostructures for excess lithium ion storage

3.1. Introduction

In order to use lithium-ion batteries as next-generation energy storage devices for electric vehicles, it is necessary to develop electrode materials having high energy density, high-speed performance and long cycle stability [3.1]. To this end, many researchers have attempted to increase the surface area and stability by applying various nanostructures to the electrode material of LIB [3.2–3.10, 3.34, 3.35].

Titanium dioxide (TiO_2) has been one of the most widely studied materials in the field of lithium ion battery cathodes. In particular, anatase TiO_2 is considered to be a candidate to replace graphite due to its environment-friendliness, low cost, and excellent stability [3.11–3.13, 3.26, 3.27, 3.33]. There have been various attempts to improve performance by applying nanostructures like other anode materials [3.14–3.21]. In particular, the nanostructured anatase has been shown to improve the long-term performance by securing the structural stability, but lithium storage was limited and only a much smaller capacity than the theoretical capacity could be demonstrated [3.11–3.13, 3.19].

The reaction of lithium with anatase takes place as an insertion mechanism and is represented by the following half-cell reaction scheme.



In this process, phase transition from anatase to $\text{Li}_{0.55}\text{TiO}_2$ occurs and the capacity is limited to 180 mAh g⁻¹ because lithium ion diffusivity is greatly reduced.

On the other hand, it has been reported that anatase crystals of sufficiently small size of 7 nm or less can store up to one lithium through an additional phase transition to LiTiO_2 by Wagemaker *et al.* in 2007. This implies the possibility of actually utilizing the theoretical capacity of anatase through nanostructures, but in reality lithium ion diffusivity on LiTiO_2 is very small, making it difficult to use it for long cycles under conventional conditions [3.22–3.25]. In this study, we report the synthesis of a hollow sphere composed of primary anatase particles with a size of several nanometers or less, so that excess lithium storage can occur stably during long cycles (228 mAh g⁻¹ in 100th cycle). We confirmed that the anatase particles of 5 nm size can store lithium by intercalation mechanism through various electrochemical analysis and in-situ analyses (X-ray diffraction (XRD) and X-ray absorption near edge structure (XANES)) by controlling the size of the nanoparticles in hollow spheres.

3.2. Experimental

It is important to examine the mechanism of the reaction through a carefully designed in-situ analysis because nanomaterials have a large impact on the electrochemical reactions, such as their shape and size. Previous studies have tended to explain the strengths of nanomaterials simply by the effect of short diffusion lengths depending on their small size. However, a more detailed analysis of how the response of actual particles differs is of great importance in explaining the electrochemical reactions of nanomaterials. Similarly for the anatase of the hollow sphere structure, it was assumed that each nanoparticle individually reacted with lithium to exhibit a nano-size effect (Fig. 3.2). It was also expected that this structure would remain stable over the long term. Four samples were prepared and analyzed to see if these concepts actually worked. We have purchased two different sizes of commercial anatase nanoparticles (TNP5 for nanoparticles with diameter of 5 nm and TNP15 for nanoparticles with diameter of 15 nm) and synthesized two types of anatase hollow spheres with different primary particle sizes (THS5 for nanoparticles with diameter of 5 nm and THS12 for nanoparticles with diameter of 12 nm). First, electrochemical performance was compared between these samples, and additional in-situ analyzes revealed that anatase nanocrystals with a size of 5 nm exert a lithium storage approaching the theoretical capacity through sequential phase transitions. This means that the particles inside the nanostructure individually exhibit the nano-size effect, and the stable capacity continues to appear through this effect during reversibly long cycles. We have designed a hollow sphere structure of small

nanoparticles to overcome the limitations of the anatase mass transfer rate and to maintain the theoretical performance over a long period of time.

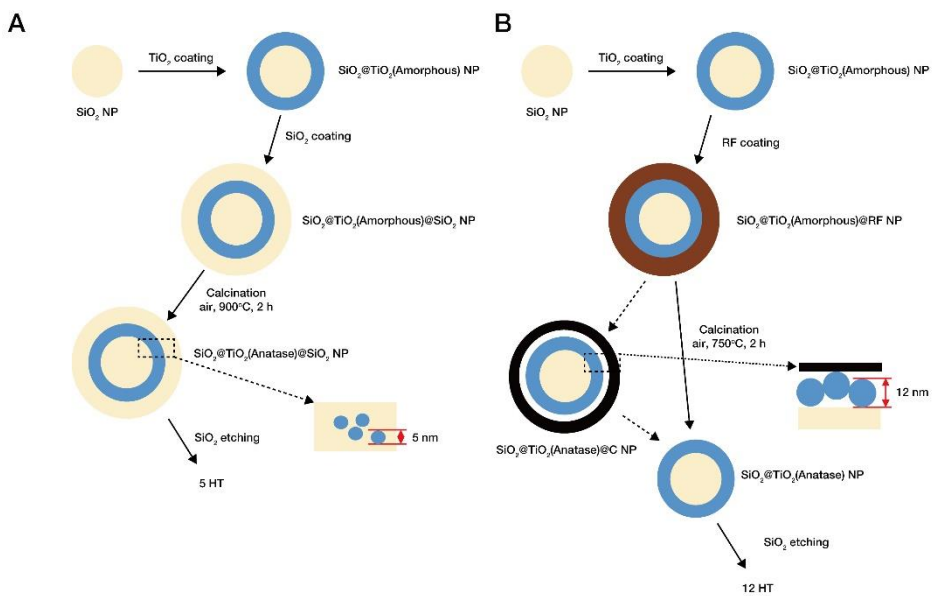


Fig. 3.1 Schematic illustration of synthesis process for hollow sphere anatase with different size of individual nanoparticles in (A) THS5 and (B) THS12.

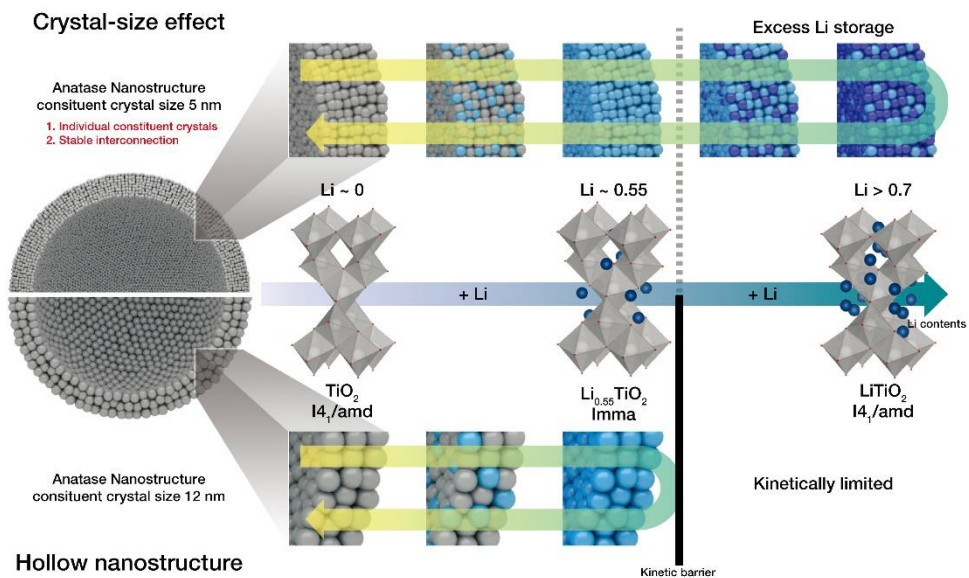


Fig. 3.2 Schematic illustration on design of anatase hollow sphere for excess lithium storage.

3.3. Results and discussion

Before the electrochemical tests, synthesized THS5 and THS12 samples were characterized by TEM and XRD (Fig. 3.3A–D, Fig. 3.4). Similarly, the commercial TNP5 and TNP15 (reference samples) were also characterized by TEM and XRD (Fig. 3.4, Fig. 3.5). THS5 and THS12 samples were prepared through a modified sacrificial template method from previously reported literature [3.28]. At first, TiO₂ shell was coated on the SiO₂ core nanoparticle uniformly by the sol-gel reaction in basic solution. Subsequently, the TiO₂-coated particles were additionally coated with SiO₂ (for THS5) or resorcinol-formaldehyde (RF, for THS12) resulting in the formation of SiO₂@TiO₂@SiO₂ or SiO₂@TiO₂@RF nanoparticles, respectively. The sizes of the constituent nanocrystals were controlled by nano-confined crystallization during high temperature calcination. Amorphous TiO₂ was crystallized into anatase TiO₂ crystals in the nano-confined region.

It has been reported that silica-protected calcination can grow anatase crystals with a size of 5 nm or less while maintaining the overall structure even at 900 °C [3.29]. In the case of RF polymer shell, when calcination is performed at 750 °C, the polymer shell is removed and grown to 12nm. In both cases, the SiO₂ core is retained rigidly, so the material synthesized in the form of a hollow sphere can be obtained, and THS5 and THS12 can be obtained by etching the SiO₂ core using an aqueous NaOH solution.

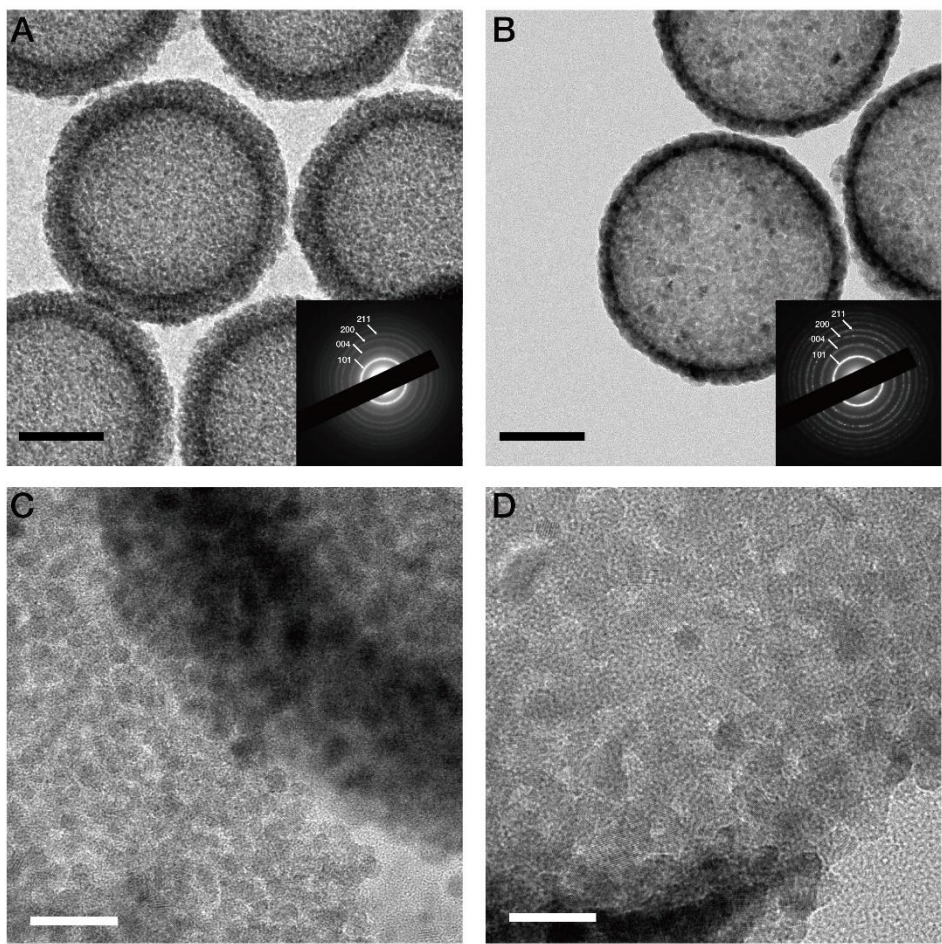


Fig. 3.3 TEM images of the synthesized anatase hollow sphere. Low magnification images of (A) THS5 and (B) THS12 (scale bar = 100 nm). The insets in A and B are the SAED patterns. High magnification images of (C) THS5 and (D) THS12 (scale bar = 20 nm).

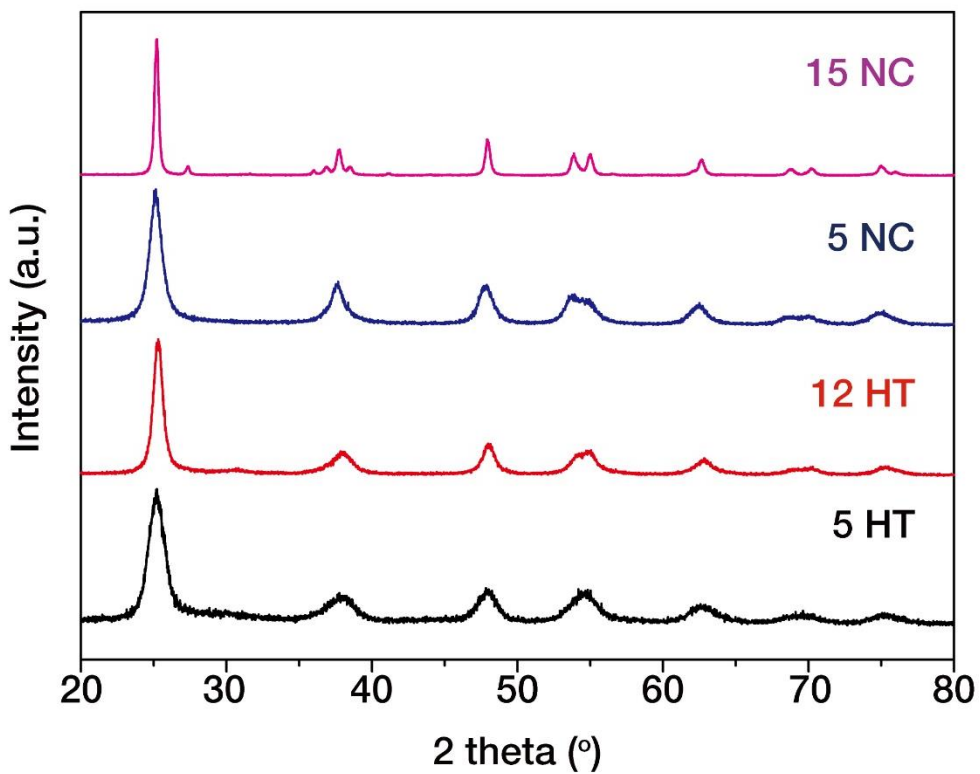


Fig. 3.4 XRD of prepared anatase nanomaterials (THS5, THS12, TNP5 and TNP15).

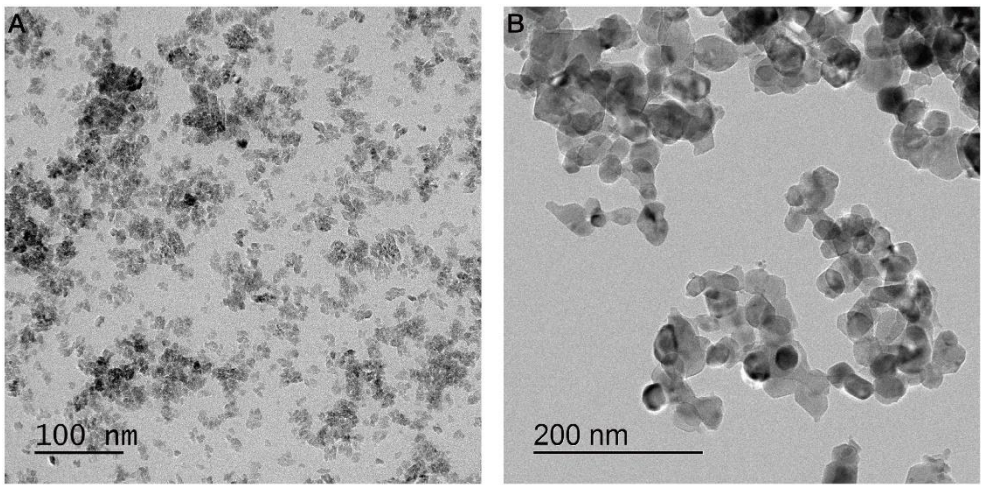


Fig. 3.5 TEM images of (A) TNP5 and (B) TNP15.

Galvanostatic lithiation was performed to investigate the effect of synergistic effect of nanostructure and crystal size on the performance of nanocrystallite anatase of hollow sphere structure as anode material of LIBs. Figure 3.6A shows the discharge capacity of the four samples and shows that anatase with hollow sphere structure maintains better capacity than conventional nanoparticles. In particular, THS5 exhibits excellent cyclic stability in addition to outstanding initial discharge capacity (330 mAh g^{-1}). It is noteworthy that this high capacity without the application of carbon composite means that anatase reacts continuously with more than 0.7 lithium ions. TNP5 shows the greatest initial capacity, but the capacity drops sharply in a few cycles. This is a phenomenon in which nanoparticles on the electrode surface lose their activity due to their disconnection, which is common when nanoparticles having no structure including TNP15 are used as the electrode material. THS12 exhibits similar capacity to other commonly reported anatases and has a somewhat lower stability than THS5. Samples with the hollow sphere structure retain their good shape retention due to their structural stability. In fact, TEM observation of THS5 after 200 cycles shows that the shape is maintained. (Fig 3.10) Due to its high structural stability, it exhibits capacities of 228 mAh g^{-1} in 100 cycles and 195 mAh g^{-1} in 500 cycles. The high-speed performance is also excellent thanks to the thin shell thickness of sufficiently small nanoparticles.

In order to determine the origin of THS5, the voltage profiles of THS5 and THS12 were divided into three voltage ranges. (Fig. 3.6C, D) In the sloping region (a) of the high voltage portion, lithium ions react with forming an anatase solid solution. In addition, the initial irreversible capacity due to the formation of solid electrolyte

interphase is also predominantly seen in this region [3.36]. In the plateau region (b), it is well known that phase transition from anatase to lithium titanate takes place through the insertion of lithium. There are two possibilities for the lithium ion reaction in the sloped region (c) of the low voltage portion. One is the pseudo-capacitive charge storage due to the large surface area of nanomaterials, which is mentioned in many studies [3.2, 3.6, 3.9, 3.32]. And the other is the crystal interstitial reaction through sequential phase transition from lithium titanate to LiTiO_2 [3.22, 3.24]. Comparing the two samples with similar nanostructures, we can observe that the ratio of region (c) is very high for THS5 to exert a much higher capacity and that the ratio remains constantly high for up to 500 cycles. Therefore, it is very important to understand exactly what happens in this area. To do this, various in-situ analysis methods were applied to measure XRD and XANES.

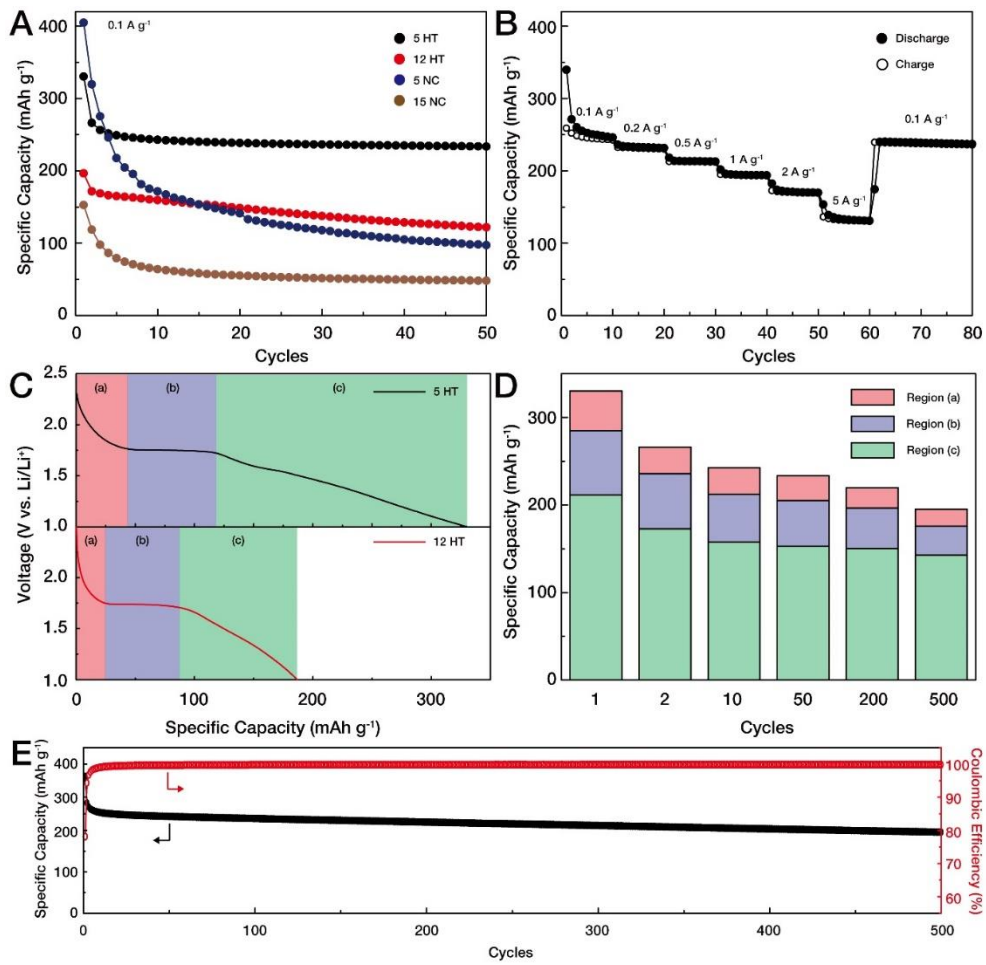


Fig. 3.6 Electrochemical results of the prepared anatase anodes. A) Cycle test of the anatase nanomaterials at 0.1 A g^{-1} (THS5, THS12, TNP5 and TNP15). B) Cycling performance of THS5 at different rates ($0.1\text{--}5 \text{ A g}^{-1}$). C) Voltage profiles of THS5 and THS12 during the first discharge. D) Ratio of capacity of three regions in THS5 during 500 cycles. E) Long-life cycle performance of THS5 at 0.1 A g^{-1} .

Table 3.1 Comparison of Li storage performance on recent anatase TiO₂ nanostructures.

Nanostructure	Initial capacity (mAh g ⁻¹ / A g ⁻¹)	Long-term capacity (mAh g ⁻¹ / A g ⁻¹ / cycle)	Rate capability (mAh g ⁻¹ / A g ⁻¹)	Ref.
Hollow	280 / 0.173*	119.5 / 0.173 / 60 127.7 / 1.73 / 1000	140.8 / 1.73	[3.10]
Decahedral plate	150 / 0.034	145 / 0.168 / 100*	79 / 2.52	[3.14]
Graphitic carbon coated hollow	225 / 0.1	178 / 0.1 / 100	151 / 1	[3.15]
Nanodisk	285.2 / 0.034	152.9 / 0.17 / 100	145 / 0.85*	[3.16]
Hollow	187.4 / 0.173	148.6 / 0.173 / 100	120.1 / 0.865	[3.17]
Nanoporous crystal	204.7 / 0.17	151.9 / 0.17 / 60	151.7 / 0.34	[3.18]
Exposed (001) facet	204 / 0.17	174 / 0.17 / 100	95 / 3.4	[3.19]
Nanofiber	220.7 / 0.04	155 / 0.04 / 100*	-	[3.20]
3D urchin-like	190 / 0.168	171 / 0.168 / 100	120 / 1.68	[3.21]
THS5	330 / 0.1	228 / 0.1 / 100 195 / 0.1 / 500	196 / 1 136 / 5	This study

*Identified from the figure

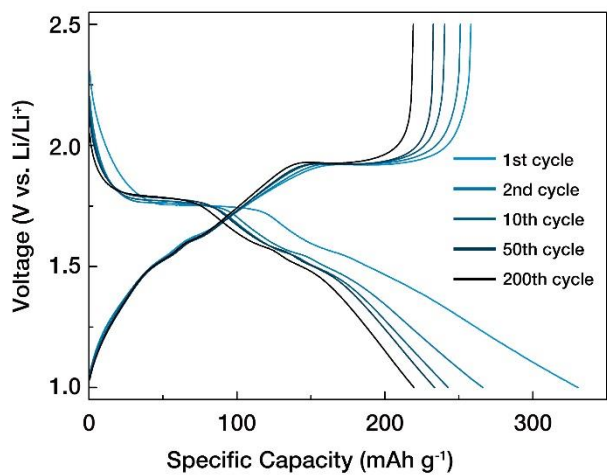


Fig. 3.7 Voltage profiles of THS5 for various cycle number.

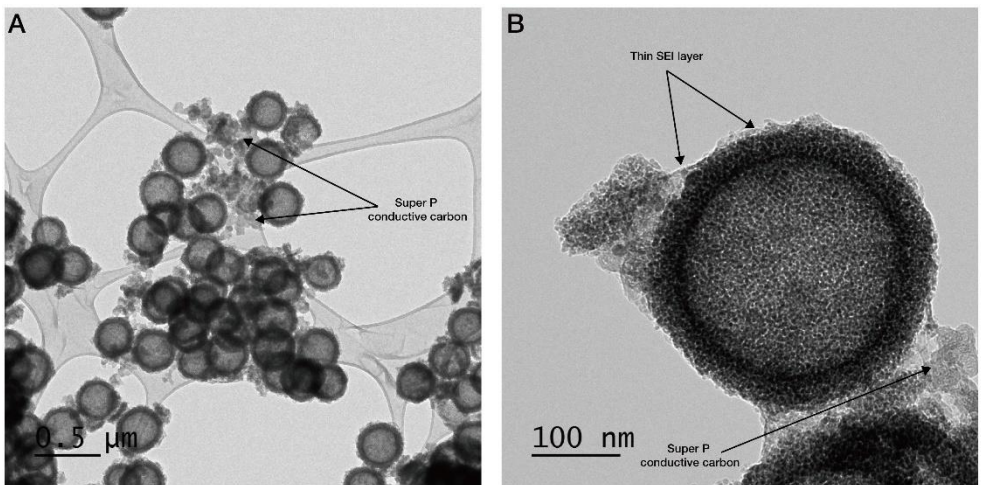


Fig. 3.8 Representative TEM images of THS5 in (A) low and (B) high magnification after the first lithium charging.

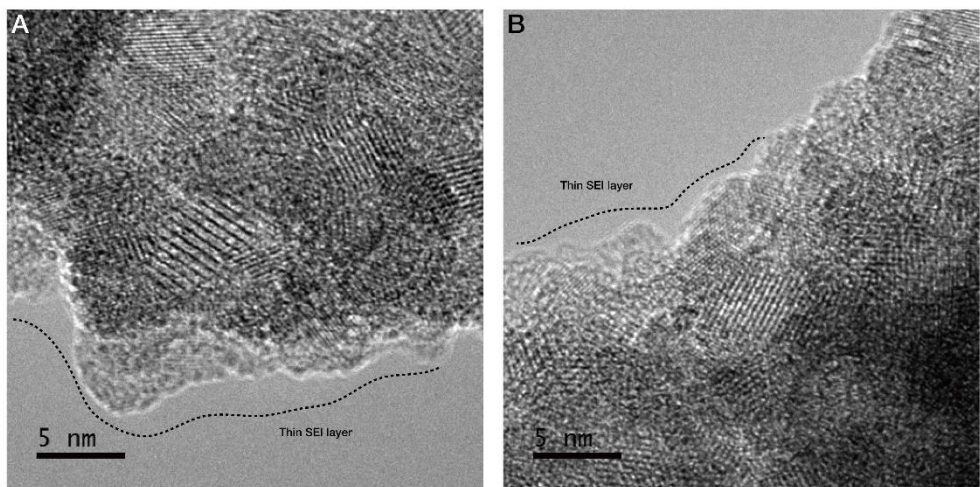


Fig. 3.9 High-resolution TEM images of THS5 indicating thin solid-electrolyte interphase (SEI) layer formation after the first lithium charging. Guided black line indicates a thin SEI layer (~2 nm) formation on the surface of THS5.

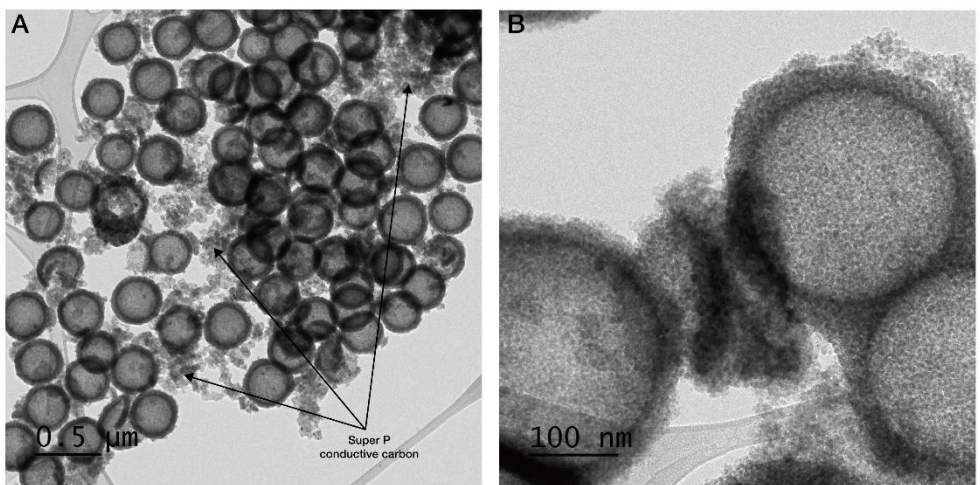


Fig. 3.10 Representative TEM images of THS5 in (A) low and (B) high magnification after 200 cycles.

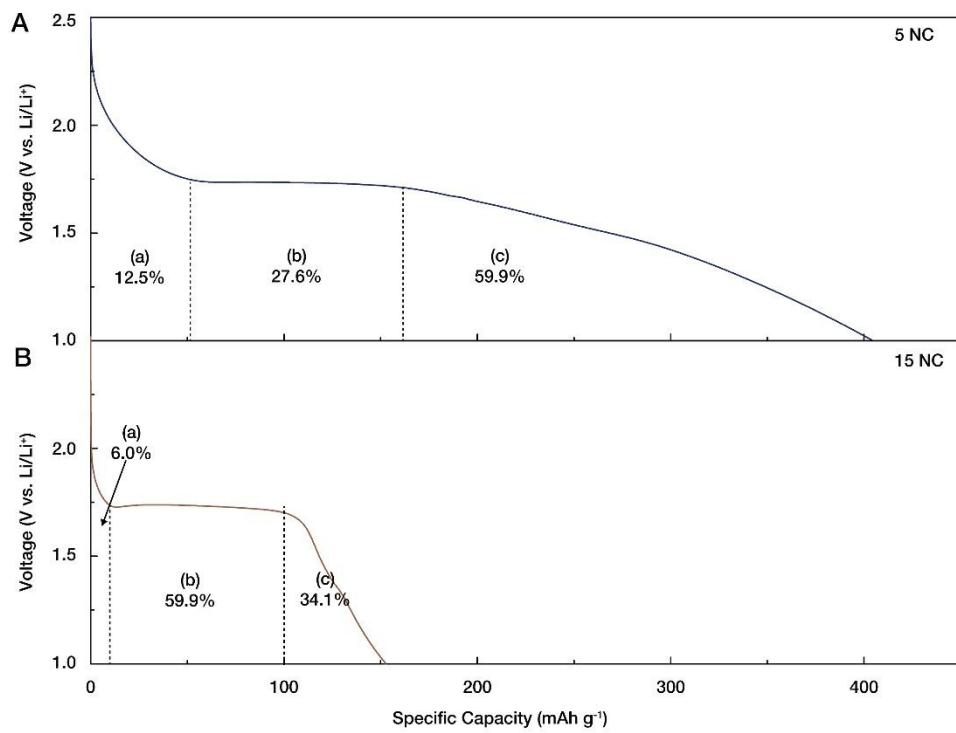


Fig. 3.11 Voltage profiles of (A) TNP5 and (B) TNP15 during the first discharge.

Fig. 3.12 shows the *in-situ* XRD results obtained for determining the reaction mechanism taking place in THS5. From the 1st cycle in the voltage profile diagram obtained through the charging and discharging in case of THS5 and THS12, it was found that in the lithiation reaction, THS5 reacts with ~0.98 lithium and THS12 reacts with ~0.55 lithium. In Fig. 3.12C, THS12 transforms from anatase into lithium titanate by reacting with 0.2 lithium (i) and maintains its crystal structure while 0.55 lithium (j) in this process. A new peak of (011) plane appears and the peak shifting of several facets (i.e. (004) and (200)) confirmed the phase transition during lithiation. During delithiation process, lithium titanate crystal structure of THS12 comes back to anatase reversibly (j→i). This is a well-known reaction, and the 12 nm constituent crystals do not exceed the kinetic barrier, thereby limiting the reaction with lithium (h→j→i). In the case of THS5, from Fig 3.12B, the lithium titanate phase appears following the reaction of ~0.4 lithium with anatase THS5 (b). The peak of (011) facet appears near 24° and the peak of (200) facet moves to lower angle also. However, THS5 exists as lithium titanate only until with ~0.75 lithium (c), and sequential phase transition occurs following reaction with more lithium. Beyond this point, peaks with the characteristic of lithium titanate disappear and a single peak appears at ~24.5° (d). This is close to the calculated peak position for the peak of (101) facet of LiTiO₂ (24.3°) after the complete lithiation reaction. LiTiO₂ has same type of crystal structure as anatase, but the lithiation reaction with lithium insertion make the unit cell parameter along the a and b axis larger. It corresponds to lower shift of the peak of (101) facet. Shifting and changing of these peaks mean the phase transition with lithiation from anatase to lithium titanate, and finally to LiTiO₂ in

series. The delithiation reaction with lithium extraction ($d \rightarrow g$) is reversible also, causing that THS5 exhibits a higher reversible capacity than conventional anatase materials due to excess lithium insertion through this additional phase transition. The first phase transition in THS5 (b, $x=0.36$) is delayed than that of the larger anatase particles (THS12, $x=0.1$) [3.13], corresponding to the result from the irreversible reaction with early lithium because of its large surface area with many defects due to small particle size. In addition, study on the reaction of lithium with anatase have reported that the solid solution region becomes longer and the phase transition occurs slower for the particles with smaller size, which is a good reference for explaining this phenomenon [3.25].

Additionally, since the same result was observed in the XRD pattern of THS5 after the 21st cycle (Fig. 3.14), this reaction is reversible and continuous. Furthermore, for the GITT results, a smaller polarization was observed for THS5 than for THS12 (Fig. 3.15), thereby demonstrating that the enhanced lithium storage of THS5 came from its excellent kinetic property. Moreover, it is memorable that THS12 exhibited higher capacity in the low voltage region (c) due to the low current and rest time during the GITT. It shows that the low capacity of THS is limited by poor kinetic properties.

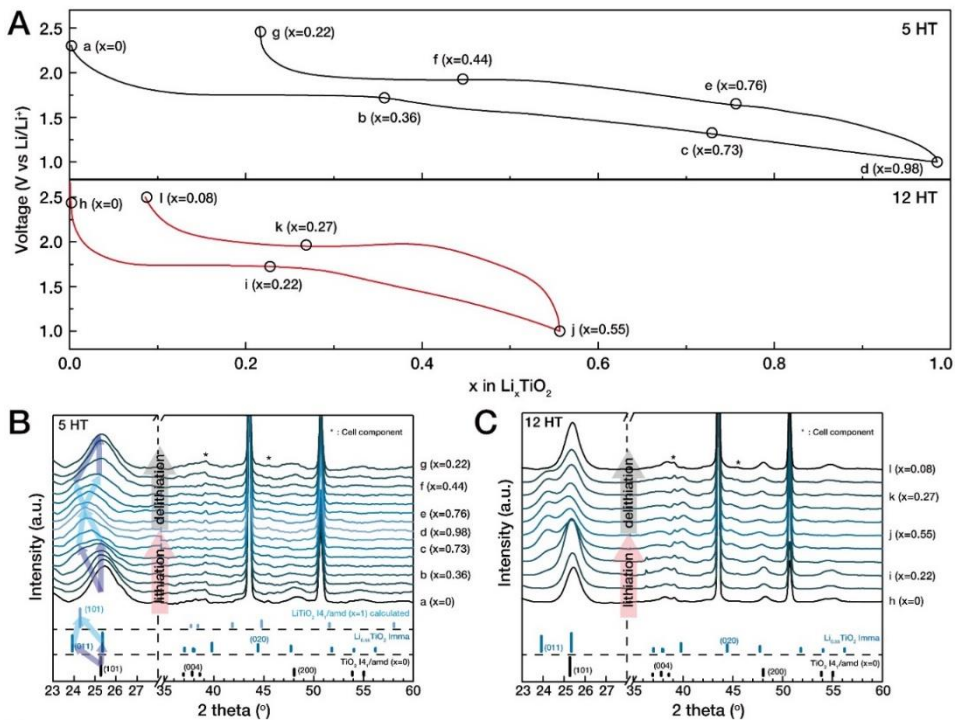


Fig. 3.12 A) Voltage profiles of THS5 and THS12 during the first cycle. B) Series of *in-situ* XRD result for THS5 in the first cycle. C) Series of *in-situ* XRD result for THS12 in the first cycle

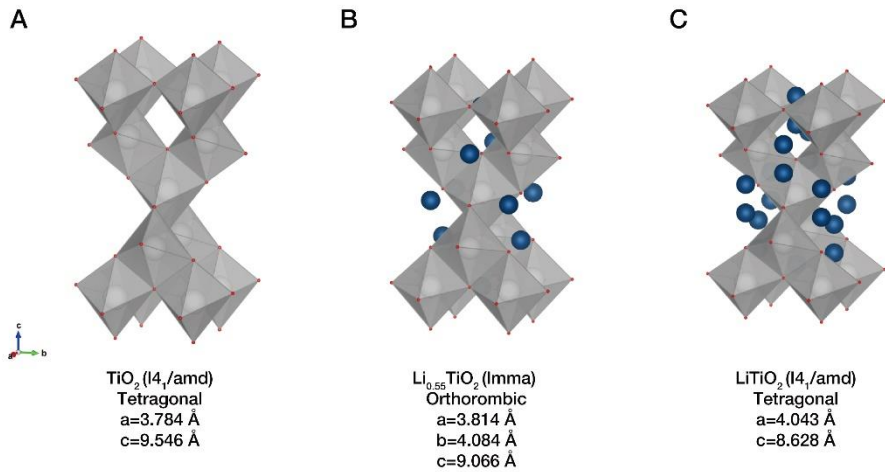


Fig. 3.13 Crystal structures of anatase TiO_2 during lithium intercalation. Each structures indicate (A) anatase, (B) lithium titanate and (C) LiTiO_2 .

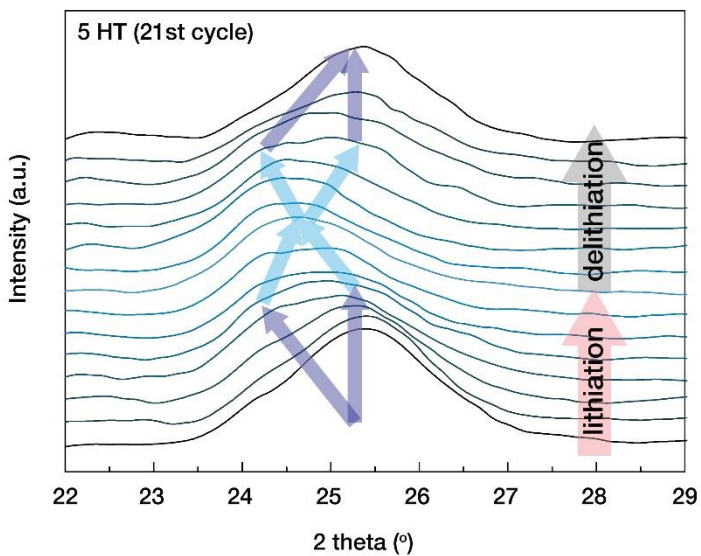


Fig. 3.14 *in-situ* XRD measurement of THS5 in 21st cycle. Similar to Fig.3.12B, sequential phase transition can be observed on constituent crystals in THS5 from anatase to LiTiO₂ through lithium titanate in 21st cycle.

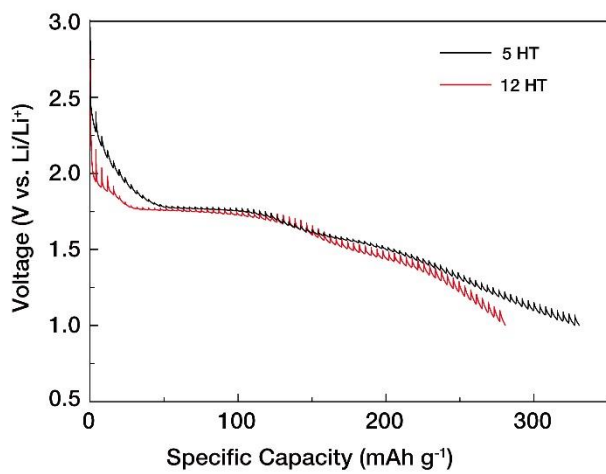


Fig. 3.15 *in operando* GITT measurement at the 1st discharge on THS5 and THS12.

GITT method was carried out with 4 mA g⁻¹ for 1 hour and rest for 2 hour.

Change in the oxidation state of the metal ion in oxide material during lithiation was confirmed by *in-situ* XANES(X-ray absorption near edge structure) to identify the reaction process (Fig 3.16). The results for THS5 show that the K-edge of Ti moves to lower energy shift during the lithiation process, thereby demonstrating that the Ti^{4+} in anatase is reduced. By plotting K-edge position of Ti with lithium contents, the linear relationship between reference anatase and Ti_2O_3 was shown in the inset of Fig. 3.16. It is therefore clear a sequential phase transition from anatase to LiTiO_2 through lithium titanate occurs during lithiation. However, the initial lithiation is partially irreversible about 0.4 lithium as mentioned above.

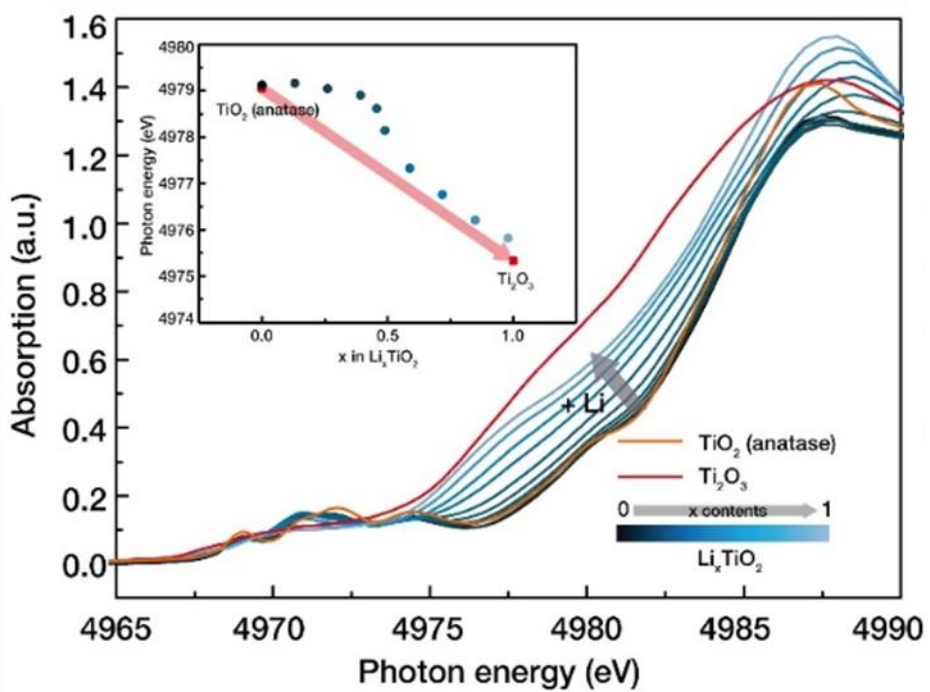


Fig. 3.16 *in-situ* XANES results for K-edge of Ti collected from the first discharge of THS5. The inset is plot of edge position with lithium contents.

3.4. Conclusion

Simultaneous control of the nanostructure and constituent crystal size of hollow anatase nanostructures allowed us to achieve higher lithium storage inside anatase TiO_2 over prolonged cycling. It was found that a sequential phase transition (anatase \rightarrow lithium titanate $\rightarrow \text{LiTiO}_2$) occurs on the individual crystals with diameter of 5 nm, and that this phenomenon can be maintained during more than 500 cycles due to the structural stability provided by hollow nanostructure. Definitely, this hollow nanostructure helps the nano-size effect maintained, leading to high capacity of 195 mAh g⁻¹ over 500 cycles, which exceeds well-known kinetic limit of anatase (\sim 180 mAh g⁻¹). In addition to the previous view that emphasize interfacial Li storage on nanostructures, our result shows that nanostructures can directly affect the lithium intercalation mechanism in crystalline anatase TiO_2 lattice, especially in long-term perspective.

Excess-lithium storage in crystal structures of various Li-active materials have been successfully demonstrated by utilizing ‘crystal-size effect’ [3-22], ‘reversible double-redox’ [3-30], and ‘anion-redox’ [3-31] mechanism. I believe this approach can also be extended on such approaches that might shed light on the development of cost-effective, stable and safe lithium-excess LIBs.

3.5. References

- [3-1] P. Poizot, S. Laruelle, S. Gruegeon, L. Dupont and J. M. Tarascon, "Nanosized transition-metal oxides as negative-electrode materials for lithium-ion batteries", *Nature*, **2000**, *407*, 496.
- [3-2] Antonino Salvatore Aricò, Peter Bruce, Bruno Scrosati, Jean-Marie Tarascon and Walter van Schalkwijk, "Nanostructured materials for advanced energy conversion and storage devices", *Nat. Mater.*, **2005**, *4*, 366.
- [3-3] Yang-Kook Sun, Zonghai Chen, Hyung-Joo Noh, Dong-Ju Lee, Hun-Gi Jung, Yang Ren, Steve Wang, Chong Seung Yoon, Seung-Taek Myung and Khalil Amine, "Nanostructured high-energy cathode materials for advanced lithium batteries", *Nat. Mater.*, **2012**, *11*, 942.
- [3-4] Myoung Hwan Oh, Taekyung Yu, Seung-Ho Yu, Byungkwon Lim, Kyung-Tae Ko, Marc-Georg Willinger, Dong-Hwa Seo, Byung Hyo Kim, Min Gee Cho, Jae-Hoon Park, Kisuk Kang, Yung-Eun Sung, Nicola Pinna and Taeghwan Hyeon, "Galvanic Replacement Reactions in Metal Oxide Nanocrystals", *Science*, **2013**, *340*, 964.
- [3-5] Ki Tae Nam, Dong-Wan Kim, Pil J. Yoo, Chung-Yi Chiang, Nonglak Meethong, Paula T. Hammond, Yet-Ming Chiang and Angela M. Belcher, "Virus-Enabled Synthesis and Assembly of Nanowires for Lithium Ion Battery Electrodes", *Science*, **2006**, *312*, 885.

[3-6] Jiangyan Wang, Hongjie Tang, Lijuan Zhang, Hao Ren, Ranbo Yu, Quan Jin, Jian Qi, Dan Mao, Mei Yang, Yun Wang, Porun Liu, Yu Zhang, Yuren Wen, Lin Gu, Guanghui Ma, Zhiguo Su, Zhiyong Tang, Huijun Zhao and Dan Wang, "Multi-shelled metal oxides prepared via an anion-adsorption mechanism for lithium-ion batteries", *Nat. Energy*, **2016**, *1*, 16050.

[3-7] Nian Liu, Zhenda Lu, Jie Zhao, Matthew T. McDowell, Hyun-Wook Lee, Wenting Zhao and Yi Cui, "A pomegranate-inspired nanoscale design for large-volume-change lithium battery anodes", *Nat. Nanotechnol.*, **2014**, *9*, 187.

[3-8] Soo Hong Lee, Seung-Ho Yu, Ji Eun Lee, Aihua Jin, Dong Jun Lee, Nohyun Lee, Hyungyung Jo, Kwangsoo Shin, Tae-Young Ahn, Young-Woon Kim, Heeman Choe, Yung-Eun Sung and Taeghwan Hyeon, "Self-Assembled Fe₃O₄ Nanoparticle Clusters as High-Performance Anodes for Lithium Ion Batteries via Geometric Confinement", *Nano Lett.*, **2013**, *13*, 4249.

[3-9] Zhiyu Wang, Liang Zhou and Xiong Wen Lou, "Metal Oxide Hollow Nanostructures for Lithium-ion Batteries", *Adv. Mater.*, **2012**, *24*, 1903.

[3-10] Bu Yuan Guan, Le Yu, Ju Li and Xiong Wen Lou, "A universal cooperative assembly-directed method for coating of mesoporous TiO₂ nanoshells with enhanced lithium storage properties", *Sci. Adv.*, **2016**, *2*,

[3-11] Seung-Ho Yu, Dong Jun Lee, Mihyun Park, Soon Gu Kwon, Hyeon Seok Lee, Aihua Jin, Kug-Seung Lee, Ji Eun Lee, Myoung Hwan Oh, Kisuk Kang, Yung-Eun Sung and Taeghwan Hyeon, "Hybrid Cellular Nanosheets for High-

Performance Lithium-Ion Battery Anodes", *J. Am. Chem. Soc.*, **2015**, *137*, 11954.

[3-12] Dawei Liu and Guozhong Cao, "Engineering nanostructured electrodes and fabrication of film electrodes for efficient lithium ion intercalation", *Energy Environ. Sci.*, **2010**, *3*, 1218.

[3-13] Guan-Nan Zhu, Yong-Gang Wang and Yong-Yao Xia, "Ti-based compounds as anode materials for Li-ion batteries", *Energy Environ. Sci.*, **2012**, *5*, 6652.

[3-14] Zhenguo Yang, Daiwon Choi, Sebastien Kerisit, Kevin M. Rosso, Donghai Wang, Jason Zhang, Gordon Graff and Jun Liu, "Nanostructures and lithium electrochemical reactivity of lithium titanites and titanium oxides: A review", *J. Power Sources*, **2009**, *192*, 588.

[3-15] M. Wagemaker, A. P. M. Kentgens and F. M. Mulder, "Equilibrium lithium transport between nanocrystalline phases in intercalated TiO₂ anatase", *Nature*, **2002**, *418*, 397.

[3-16] S. Y. Huang, L. Kavan, I. Exnar and M. Grätzel, "Rocking Chair Lithium Battery Based on Nanocrystalline TiO₂ (Anatase)", *J. Electrochem. Soc.*, **1995**, *142*, L142.

[3-17] Tsutomu Ohzuku, Takahiro Kodama and Taketsugu Hirai, "Electrochemistry of anatase titanium dioxide in lithium nonaqueous cells", *J. Power Sources*, **1985**, *14*, 153.

- [3-18] Xiao Hua, Zheng Liu, Michael G. Fischer, Olaf Borkiewicz, Peter J. Chupas, Karena W. Chapman, Ullrich Steiner, Peter G. Bruce and Clare P. Grey, "Lithiation Thermodynamics and Kinetics of the TiO₂ (B) Nanoparticles", *J. Am. Chem. Soc.*, **2017**, *139*, 13330.
- [3-19] Ping Niu, Tingting Wu, Lei Wen, Jun Tan, Yongqiang Yang, Shijian Zheng, Yan Liang, Feng Li, John T. S. Irvine, Gang Liu, Xiuliang Ma and Hui-Ming Cheng, "Substitutional Carbon-Modified Anatase TiO₂ Decahedral Plates Directly Derived from Titanium Oxalate Crystals via Topotactic Transition", *Adv. Mater.*, **2018**, *30*, 1705999.
- [3-20] Hao Liu, Wei Li, Dengke Shen, Dongyuan Zhao and Guoxiu Wang, "Graphitic Carbon Conformal Coating of Mesoporous TiO₂ Hollow Spheres for High-Performance Lithium Ion Battery Anodes", *J. Am. Chem. Soc.*, **2015**, *137*, 13161.
- [3-21] Gonu Kim, Changshin Jo, Wooyul Kim, Jinyoung Chun, Songhun Yoon, Jinwoo Lee and Wonyong Choi, "TiO₂ nanodisks designed for Li-ion batteries: a novel strategy for obtaining an ultrathin and high surface area anode material at the ice interface", *Energy Environ. Sci.*, **2013**, *6*, 2932.
- [3-22] Genqiang Zhang, Hao Bin Wu, Taeseup Song, Ungyu Paik and Xiong Wen Lou, "TiO₂ Hollow Spheres Composed of Highly Crystalline Nanocrystals Exhibit Superior Lithium Storage Properties", *Angew. Chem. Int. Ed.*, **2014**, *53*, 12590.
- [3-23] Jianfeng Ye, Wen Liu, Jinguang Cai, Shuai Chen, Xiaowei Zhao, Henghui

Zhou and Limin Qi, "Nanoporous Anatase TiO₂ Mesocrystals: Additive-Free Synthesis, Remarkable Crystalline-Phase Stability, and Improved Lithium Insertion Behavior", *J. Am. Chem. Soc.*, **2011**, *133*, 933.

[3-24] Jun Song Chen, Yi Ling Tan, Chang Ming Li, Yan Ling Cheah, Deyan Luan, Srinivasan Madhavi, Freddy Yin Chiang Boey, Lynden A. Archer and Xiong Wen Lou, "Constructing Hierarchical Spheres from Large Ultrathin Anatase TiO₂ Nanosheets with Nearly 100% Exposed (001) Facets for Fast Reversible Lithium Storage", *J. Am. Chem. Soc.*, **2010**, *132*, 6124.

[3-25] Sangkyu Lee, Wonsik Eom, Hun Park and Tae Hee Han, "High-Temperature Stable Anatase Titanium Oxide Nanofibers for Lithium-Ion Battery Anodes", *ACS Appl. Mater. Interfaces*, **2017**, *9*, 25332.

[3-26] Muhammad Saad Salman, A. Reum Park, Min Jin Cha, Youngjin Choi, Sung Kyu Jang, Lihan Tan, Pil J. Yoo and Woo-Seok Choe, "Lysozyme-Templated Meso-Macroporous Hollow TiO₂ for Lithium Ion Battery Anode", *ACS Appl. Nano Mater.*, **2018**, *1*, 698.

[3-27] Marnix Wagemaker, Wouter J. H. Borghols and Fokko M. Mulder, "Large Impact of Particle Size on Insertion Reactions. A Case for Anatase Li_xTiO₂", *J. Am. Chem. Soc.*, **2007**, *129*, 4323.

[3-28] W. J. H. Borghols, D. Lutzenkirchen-Hecht, U. Haake, E. R. H. van Eck, F. M. Mulder and M. Wagemaker, "The electronic structure and ionic diffusion of nanoscale LiTiO₂ anatase", *PCCP*, **2009**, *11*, 5742.

[3-29] U. Lafont, D. Carta, G. Mountjoy, A. V. Chadwick and E. M. Kelder, "In Situ Structural Changes upon Electrochemical Lithium Insertion in Nanosized Anatase TiO₂", *J. Phys. Chem. C*, **2010**, *114*, 1372.

[3-30] Kun Shen, Hao Chen, Frits Klaver, Fokko M. Mulder and Marnix Wagemaker, "Impact of Particle Size on the Non-Equilibrium Phase Transition of Lithium-Inserted Anatase TiO₂", *Chem. Mater.*, **2014**, *26*, 1608.

[3-31] Niek J. J. de Klerk, Alexandros Vasileiadis, Raymond B. Smith, Martin Z. Bazant and Marnix Wagemaker, "Explaining key properties of lithiation in TiO₂-anatase Li-ion battery electrodes using phase-field modeling", *Phys. Rev. Materials*, **2017**, *1*, 025404.

[3-32] Hongyan Liu, Ji Bong Joo, Michael Dahl, Lishun Fu, Zhengzhi Zeng and Yadong Yin, "Crystallinity control of TiO₂ hollow shells through resin-protected calcination for enhanced photocatalytic activity", *Energy Environ. Sci.*, **2015**, *8*, 286.

[3-33] Chunhai Jiang, Mingdeng Wei, Zhimei Qi, Tetsuichi Kudo, Itaru Honma and Haoshen Zhou, "Particle size dependence of the lithium storage capability and high rate performance of nanocrystalline anatase TiO₂ electrode", *J. Power Sources*, **2007**, *166*, 239.

[3-34] Ji-Yong Shin, Dominik Samuelis and Joachim Maier, "Sustained Lithium-Storage Performance of Hierarchical, Nanoporous Anatase TiO₂ at High Rates: Emphasis on Interfacial Storage Phenomena", *Adv. Funct. Mater.*, **2011**, *21*,

3464.

[3-35] Jinhyuk Lee, Daniil A. Kitchev, Deok-Hwang Kwon, Chang-Wook Lee, Joseph K. Papp, Yi-Sheng Liu, Zhengyan Lun, Raphaële J. Clément, Tan Shi, Bryan D. McCloskey, Jinghua Guo, Mahalingam Balasubramanian and Gerbrand Ceder, "Reversible Mn²⁺/Mn⁴⁺ double redox in lithium-excess cathode materials", *Nature*, **2018**, *556*, 185.

[3-36] M. Sathiya, G. Rousse, K. Ramesha, C. P. Laisa, H. Vezin, M. T. Sougrati, M. L. Doublet, D. Foix, D. Gonbeau, W. Walker, A. S. Prakash, M. Ben Hassine, L. Dupont and J. M. Tarascon, "Reversible anionic redox chemistry in high-capacity layered-oxide electrodes", *Nat. Mater.*, **2013**, *12*, 827.

[3-37] Xiaojing Wang, Ji Feng, Yaocai Bai, Qiao Zhang and Yadong Yin, "Synthesis, Properties, and Applications of Hollow Micro-/Nanostructures", *Chem. Rev.*, **2016**, *116*, 10983.

[3-38] Xiaoyong Lai, Jonathan E. Halpert and Dan Wang, "Recent advances in micro-/nano-structured hollow spheres for energy applications: From simple to complex systems", *Energy Environ. Sci.*, **2012**, *5*, 5604.

[3-39] Changshin Jo, Youngsik Kim, Jongkook Hwang, Jongmin Shim, Jinyoung Chun and Jinwoo Lee, "Block Copolymer Directed Ordered Mesostructured TiNb₂O₇ Multimetalllic Oxide Constructed of Nanocrystals as High Power Li-Ion Battery Anodes", *Chem. Mater.*, **2014**, *26*, 3508.

국문초록

리튬이온전지 음극 물질인 실리콘과 티타늄 산화물의 설계 및 분석

리튬이온전지는 양 전극 물질 내의 리튬 이온의 화학적 퍼텐셜 차이를 이용해 전기에너지와 화학에너지를 서로 전환하는 에너지 전환/저장 장치이다. 높은 에너지밀도를 갖는 장점으로 인해 많은 휴대기기의 전원장치로 사용되고 있으며 전기자동차의 수요가 늘어남에 따라 더욱 높은 성능이 요구되기 때문에 성능 향상을 위해 많은 연구가 이뤄지고 있다. 많은 연구자들이 주목하는 부분은 더 높은 에너지밀도를 얻기 위해 더 큰 용량을 가지는 전극물질을 개발하는 것이다. 현재 상업적으로 사용되고 있는 전극물질인 흑연과 리튬코발트산화물을 대신하기 위해 더 높은 비용량을 갖는 물질을 이용하려면 몇 가지 과제를 해결해야 한다. 높은 용량을 갖는 합금 또는 전환 반응 물질의 경우 많은 리튬과의 반응으로 인한 부피 팽창과 새로운 화학결합으로 인한 구조적 불안이 가장 큰 문제이며, 다양한 구조를 적용해 안정성을 확보하는 방향으로 연구가 진행되고 있다. 한편 리튬과의 반응이

안정적인 삽입반응 물질은 추가적인 용량을 확보하기 위해 표면을 개질하거나 나노구조를 적용하는 연구가 진행되고 있다. 이러한 방법들 중 가장 많이 시도되는 것은 전극물질에 다공성 구조를 적용함으로써 구조적 안정성을 강화시킴과 동시에 넓어진 표면적으로 인한 우수한 속도특성을 얻어내는 것이다. 더 나아가서 전극물질의 특성에 맞는 다공성 구조를 설계하여 적용시키면 최적화된 성능을 얻어낼 수 있을 것이라고 기대할 수 있다.

이 연구에서는 먼저 실리콘을 리튬이온전지 음극으로 효율적으로 사용하기 위해 다공성 구조를 적용하려고 시도했다. 다공성 실리콘을 손쉽게 얻을 수 있는 방법으로 잘 알려진 magnesiothermic 반응은 마그네슘의 환원력을 이용해 실리카를 다공성 실리콘으로 만드는 반응이다. 이 과정에서 마그네슘 실리사이드가 반응 중간체로 작용한다는 점에 착안하여 실험을 진행한 결과 이것이 실리카 뿐 아니라 다른 4족 원소의 산화물(이산화탄소, 산화 게르마늄, 산화 주석)들 역시 원활하게 환원시킬 수 있다는 것을 알아냈다. 이 반응을 통해 다공성 실리콘과 다른 물질의 복합체를 합성할 수 있었으며 이러한 구조가 실리콘의 안정성에 도움을 주는 것을 확인할 수 있었다. 이에 더불어 시작 물질을 주변에서 쉽게 얻을 수 있는 모래로 설정함으로써 실제 산업에서 응용될 가능성을 열었을 뿐 아니라 빈 공간을 추가적으로 확보해 실리콘/탄소 복합체의 용량이 200 싸이클에서 1000 mAh g^{-1} 을

넘는 성능 향상 또한 이를 수 있었다.

연구의 나머지 부분에서는 아나타제 상의 이산화티타늄이 갖는 한계를 극복하기 위해 다공성 구조를 적용했다. 아나타제 이산화티타늄은 이론적으로 한개까지의 리튬과 반응하여 330 mAh g^{-1} 의 용량을 발휘할 수 있다고 알려져 있으나 내부 격자에 0.5개의 리튬이 들어가 티탄산 리튬으로 상전이가 일어나게 되면 물질 내부의 리튬이온 확산이 크게 저하되어 더 이상 반응이 진행되지 않는다. 그러나 7나노미터 미만의 충분히 작은 크기의 나노입자를 이용하게 되면 이 속도장벽을 극복할 수 있다는 것이 잘 알려져 있고, 실제로 5나노미터 크기의 개별 입자들로 이루어진 속이 비어있는 구 형태의 아나타제 이산화티타늄을 리튬이온전지 전극물질로 활용한 결과 330 mAh g^{-1} 의 높은 초기용량을 발휘하였으며 안정된 구조 덕분에 500사이클에서 195 mAh g^{-1} 라는 우수한 장기 성능을 보였다. 또한 높은 용량을 발휘하는 이유가 흔히 알려진 표면반응이 아닌 이산화티타늄 격자 내부로 리튬이온이 삽입되며 발생하는 추가적인 상전이라는 것을 다양한 제자리 분석을 통해 확인할 수 있었다.